



Control of landslide retrogression by discontinuities: evidences by the integration of airborne- and ground-based geophysical information

Julien Travelletti, Jean-Philippe Malet, Kevin Samyn, Gilles Grandjean,
Michel Jaboyedoff

► To cite this version:

Julien Travelletti, Jean-Philippe Malet, Kevin Samyn, Gilles Grandjean, Michel Jaboyedoff. Control of landslide retrogression by discontinuities: evidences by the integration of airborne- and ground-based geophysical information. *Landslides*, 2013, 10 (1), pp.37-54. 10.1007/s10346-011-0310-8. hal-00649682

HAL Id: hal-00649682

<https://hal-brgm.archives-ouvertes.fr/hal-00649682>

Submitted on 8 Dec 2011

HAL is a multi-disciplinary open access archive for the deposit and dissemination of scientific research documents, whether they are published or not. The documents may come from teaching and research institutions in France or abroad, or from public or private research centers.

L'archive ouverte pluridisciplinaire **HAL**, est destinée au dépôt et à la diffusion de documents scientifiques de niveau recherche, publiés ou non, émanant des établissements d'enseignement et de recherche français ou étrangers, des laboratoires publics ou privés.

Control of landslide retrogression by discontinuities: evidences by the integration of airborne- and ground-based geophysical information

J. Travelletti (1, 2), J.-P. Malet (1), K. Samyn (3), G. Grandjean (3), M. Jaboyedoff (4)

¹ *Institut de Physique du Globe de Strasbourg, CNRS UMR 7516, University of Strasbourg (EOST), 5 rue René Descartes, F-67084 Strasbourg Cedex, France (julien.travelletti@unistra.fr; Phone: +33 (0)3 90 85 01 14)*

² *GEOPHEN - LETG, CNRS UMR 6554, University of Caen Basse-Normandie, F-14032 Caen Cedex, France*

³ *BRGM, Bureau des Recherches Géologiques et Minières, 3 Avenue Guillemin, F-45100 Orléans, France*

⁴ *IGAR, Institute of Geomatics and Analysis of Risk, University of Lausanne, CH-1015 Lausanne, Switzerland*

Abstract The objective of this work is to present a multi-technique approach to define the geometry, the kinematics and the failure mechanism of a retrogressive large landslide (upper part of the La Valette landslide, South French Alps) by the combination of airborne (ALS) and terrestrial (TLS) laser scanning data and ground-based seismic tomography data. The advantage of combining different methods is to constrain the geometrical and failure mechanism models by integrating different source of information.

Because of an important point density at the ground surface (4.1 pt.m^{-2}), a small laser footprint (0.09 m) and an accurate 3D positioning (0.07 m), ALS data are adapted source of information to analyze morphological structures at the surface. Seismic tomography surveys (P-wave and S-wave velocities) may highlight the presence of low seismic-velocity zones which characterize the presence of dense fracture networks at the sub-surface. The surface displacements measured from TLS data over a period of two years (May 2008-May 2010) allow one to quantify the landslide activity at the direct vicinity of the identified discontinuities. An important subsidence of the crown area with an average subsidence rate of 3.07 m.year^{-1} is determined. The displacement directions indicate that the retrogression is controlled structurally by the pre-existing discontinuities.

A conceptual structural model is proposed to explain the failure mechanism and the retrogressive evolution of the main scarp. Uphill, the crown area is affected by planar sliding included in a deeper wedge failure system constrained by two pre-existing fractures. Downhill, the landslide body acts as a buttress for the upper part. Consequently, the progression of the landslide body downhill allows the development of dip-slope failures and coherent blocks start sliding along

planar discontinuities. The volume of the failed mass in the crown area is estimated at 500,000 m³ with the Sloping Local Base Level method.

Keywords:

Slope failure, ALS data, TLS data, Seismic tomography, Discontinuity, Geological model

Introduction

A challenge to progress in landslide research is to define the geometry of the failed mass and the possible failure mechanism precisely in order to better forecast their spatial and temporal pattern of development. From a geological point of view, unstable slopes affected by landslides can be broadly divided into strong rock-types and soft rock-types of failure (according to the ISRM classification of rock and soil strength; ISRM, 1981; Hoek and Bray, 2004) with a transitional evolution among these two broad categories. In most strong rock slopes, pre-existing discontinuities control the landscape morphology. As a consequence, unfavorable small-scale pre-existing fractures are often the main predisposing factors of large landslides (Cruden, 1976; Agliardi et al., 2001; Sartori et al., 2003; Hoek and Bray, 2004; Eberhardt et al., 2005; Jaboyedoff et al., 2009). In soft rock slopes (e.g. weakly cemented sedimentary units such as highly weathered and fractured rocks, conglomerates, sandstones and clays), the heritage of pre-existing structures can also play an essential role on the failure mechanisms. For example, Irfan (1998) showed that the slope behaviour in saprolitic soil is controlled not only by the weathered material itself but also by relict discontinuities, particularly when these are unfavorably oriented with respect to the slope face. Undercut slopes affected by buttress removal are among the typical failure mechanisms that occur in soft rocks, leading to the development of shear zones at depth (Leroueil 2001; Cruden and Martin 2004).

In landslide investigations, a combination of several direct and indirect techniques is very often used, and several complementary ground-based and airborne-based technologies have been developed in the last decade to provide spatially-distributed information about the structure. In combination with field observations and classical geotechnical investigation, the ground-based techniques are mainly 2D and 3D electrical resistivity and seismic tomographies (Jongmans and Garambois 2007) and the airborne-based techniques are mainly radar interferometry techniques (InSAR), Light Detection and Ranging techniques (LiDAR) and correlation of optical imageries (Travelletti et al., in press; Jaboyedoff et al., 2009). Terrestrial Laser Scanning (TLS) and Airborne Laser Scanning (ALS) are very efficient techniques for characterizing the morpho-structure (Feng and Röshoff, 2004; Slob and Hack, 2004; Jaboyedoff et al., 2009) and the kinematics of landslides (Rosser et al., 2007; Monserrat and Crosetto 2008; Travelletti et al., 2008; Prokop and Panholzer 2009) because they provide a rapid collection of field topographical data with a high density of points within a range of several hundreds of meters. Possible mechanisms affecting the slope can then be estimated from the displacement vectors at the ground surface (Crosta and Agliardi, 2003; Jaboyedoff et al., 2004a) such as the geometry of the slip surface (Casson et al., 2005; Travelletti et al., 2008; Oppikofer et al., 2009).

In strong rock-types of failure, the morpho-structures identified at the ground surface often reflect the internal geometry of the deformation (Agliardi et al., 2001; Eberhardt et al., 2005). The extensions of persistent structures in depth are more difficult to identify in soft rocks because these lithologies are very often affected by low persistence, closely spaced joints that occur in a wide variety of orientations. The landslide kinematics in soft rock can be both controlled by regional discontinuities and recent internal failure surface under development in the rock mass (Irfan, 1998). The development of new circular or planar failures which partly encompass the intact rock is therefore possible as observed, for example, in weathered basalts or sandstones (Hoek and Bray, 2004). Another example

of weak rocks is evaporites lithology that is particularly exposed to dissolution processes. They generally form smooth topographies at small scale which make the identification of regional discontinuities difficult from morpho-structure analyses at the ground surface or through DEMs (Travelletti et al., 2010). Additional surveys are thus necessary to complement this lack of information in depth.

In the last decade, the applications of seismic tomographies for landslide investigations showed that S and P-wave velocities are of interest techniques to characterize properties such as the layering, the degree of fracturing and the stiffness of the material (Grandjean et al., 2006; Jongmans et al., 2009). The internal strain affecting soft-rock landslides usually induces a velocity contrast between the unstable mass and the stable bedrock (Caris and van Asch, 1991, Méric et al., 2007; Jongmans and Garambois, 2007). Grandjean et al. (2006) showed that seismic velocities are much more sensitive to the degree of fracturing than the electrical resistivity tomography techniques (ERT) which complement geological and geomorphological assessments.

Still, a major difficulty consists in interpreting and integrating all the available data in a coherent framework to provide a complete picture of the landslide structure.

This work presents a multi-technique approach to characterize the structure of the upper part of the La Valette landslide (South French Alps) by combining high-resolution seismic tomographies, airborne and terrestrial LiDAR surveys (ALS, TLS) and geomorphological analyses. First, the geomorphological and historical setting of the landslide is presented; then the methodology used to analyse the multi-source data is detailed and the Sloping Local Base Level (SLBL) method is applied to estimate the landslide volume. Finally a kinematic model explaining the failure mechanism in the upper part of the landslide is proposed and discussed.

Geomorphological and historical features of the La Valette landslide

The La Valette landslide, originated in 1982, is one of the most important large and complex slope movements in the South French Alps. The landslide associates two styles of activity: a mudslide type of behavior with the development of a flow tongue in the medium and lower part, and a slump type of behavior with the development of several rotational and planar slides in the upper part at the main scarp. The landslide extends over a length of 2 km for a variable width of 0.2 km in the lower and medium parts, to 0.5 km in the upper part (Fig. 1a). The maximum depth, estimated by seismic and electrical resistivity tomography and geotechnical boreholes, varies from 25 m in the lower and middle parts (Evin 1992; Travelletti et al., 2009) to 35 m in the upper part (Le Mignon 2004). The mean slope gradient is ca. 30° in the scarp area and ca. 20° in the mudslide area (Fig. 1b). The volume of the landslide body is estimated at $3.5 \times 10^6 \text{ m}^3$.

The landslide affects a hillslope located uphill of the municipality of Saint-Pons (Alpes-de-Haute-Provence), and poses a significant threat for the 170 community housings located downstream (Le Mignon and Cojean 2002). The occurrence of rapid mudflows triggered from the landslide body and in the scarp area in the 1980s and 1990s conducted to the development of an early-warning system since 1991 composed of a survey network of benchmarks, optical and infra-red camera monitoring and the installation debris height detection sensors in the run-out channel, and the drainage of the lower part of the landslide.

Geological setting

From a geological viewpoint, the La Valette landslide is located at the overthrust fault between two major lithologies outcropping in the geologic window of the Barcelonnette basin (South-east France; Fig. 2a):

- An autochthonous formation represented by the closely stratified Callovo-Oxfordian black marls (e.g. “Terres Noires”) and characterized by a typical landscape of badlands. This formation is located in the middle and the lower parts of the slope. The bedding plane is characterized with a decametric alternance of carbonate beddings within the marls. This formation dips constantly towards 083° with an inclination of 23° in the landslide surroundings;

- An allochthonous formation represented by two nappes and in which the upper part of the landslide has developed. The basal nappe is a tectonic wedge belonging to the Pelat Nappe and is composed of highly fractured flysch and planctonic carbonates of the Turonian and Paleocene Superior age (BRGM 1974). This formation has a few dozen of meters of thickness at the location of the main scarp with an average dip direction and dip of 135°/30°. The Pelat Nappe is overlaid by the upper Autapie Nappe composed of highly fractured Helminthoïd flyschs, sandstones, marls and schists. This formation is dated at the Upper Cretaceous–Upper Eocene (BRGM 1974). The tectonic discordance between the autochthonous and the allochthonous (052°/16°) materializes the major thrust fault delimiting the Barcelonnette basin, and constitutes a weak zone where many landslide source areas are located (Le Mignon 2004). Generally, the bedding plane, the fold axes and the schistosity are very difficult to identify with certainty at the outcrop scale due to the high variability of the orientation measurements and the bad rock mass quality which does not ensure that the rock outcrop is in place. Therefore, the small-scale geological observations of persistent structures carried out in the field indicate only the regional structural and tectonic patterns and cannot directly be integrated in a local geological model of discontinuities.

164 **Hydro-geological setting**

From a hydro-geological viewpoint, the tectonic discordance has an important role on the landslide hydrology. Due to the high heterogeneity of the landslide material and of the highly dislocated texture of the flysch, both materials are considered as aquifers at the scale of the landslide. At the opposite, the black marls formation is considered as an aquitard (Dupont and Taluy 2000; Le Mignon 2004). Consequently, the contrast of permeability between the black marls and the flysch controls the spatial occurrence of several springs and marshy areas observed in the direct vicinity of the overthrust fault between the elevation 1870 m and 1950 m (Fig. 2a, 2b). According to Le Mignon (2004), a spring (the “Rocher Blanc” spring at 1900 m) is currently partially buried by the landslide. Consequently a deep water circulation affects the hydrological regime of the upper part of the landslide but the characteristics of the water flows (fluxes, quality) are unknown. Near the North West boundary of the landslide, springs are remarkably aligned at the elevation 1880 m. They are likely connected to the Rocher Blanc spring through a discontinuity buried by the landslide. Remediation works were built by the local stakeholders in charge of the prevention (Service of “Restauration des Terrains de Montagne”, RTM) in order to drawdown and buffer the hydraulic heads within the landslide. Sub-horizontal drains below the major overthrust fault were installed in the 1990s, but their maintenance was too difficult due to the rapid shearing of the tubes. The most efficient mitigation solution has been the installation of shallow drainage systems in the middle and lower parts of the landslide to impede streaming water to infiltrate the landslide.

186 **Landslide historical and recent development**

The landslide exhibits a complex style of activity in space and time. It has developed first as a rotational slide affecting the Autapie Nappe in relation to a major overthrust fault following important rainfalls favoring fast snow melting (Colas and Locat 1993; Le Mignon 2004). The failed mass has progressively loaded the underlying black marls formation, and the landslide has developed by a series of rapid mudflows triggered in the

marls such as in March 1982, April 1988, March 1989 and March 1992. The most important acceleration occurred in 1988 when a mudflow of 50.000 m³ triggered at the elevation of 1400 m propagates over a runout distance of ca. 500 m (Colas and Locat 1993). Up to now, these mudflows did not mobilize the complete failed mass. The displacements are monitored with topometric benchmarks since 1991 (Squarzoni et al., 2005), differential dual-frequency GPS (Déprez et al., submitted) and an extensometer since 2008, and at regular periods by digital correlation of satellite images (Le Prince 2008) and satellite radar interferometry (Squarzoni et al., 2003).

Two main aspects can be pointed out from these studies and from the observations by the local stakeholders. The first one is the decrease of velocity (from 0.4 m.day⁻¹ to about 0.01 m.day⁻¹) in the middle and lower part of the landslide caused by the local groundwater drawdown since the installation of a drainage system in the 1990s. The second is the important activity since the year 2000 of the upper part at the Soleil Boeuf crest, which is characterized by a rapid retrogression of the main scarp towards the North-East and an enlargement of the landslide towards the North-West (Fig. 3). In response to this worrying situation, the RTM Service has installed several additional benchmarks along profiles both in the unstable and stable parts of the Soleil-Boeuf crest to monitor the displacements in the crown area (Fig. 1b, Fig. 4). Actually, an accumulation of material and a steepening of the slope are observed in the upper part of the landslide because of the retrogression of the scarp. Consequently, the possible hazard scenario consists in the undrained loading of underlying black marls formation and the triggering of new rapid and mobile mudflows.

Methodology

The recent increase of activity in the crown and in the main scarp areas has motivated further investigations to define the possible volume of material still able to fail, and to better understand the failure mechanisms in that part of the slope. Geological observations, small-scale morpho-structural analysis with ALS data, large-scale kinematical analysis with TLS data and a morpho-structural analysis in depth with seismic tomographies have been carried out since 2008 (Fig. 1b, Fig. 4).

Geological observations of the discontinuities in the main scarp and in the crown areas

Field investigations in the scarp area are focused on the identification and the orientation of the major morpho-structures and discontinuities measured with a geological compass and mapped with a differential GPS. The landslide scarp is characterized by slopes ranging from 25° to 55° over a maximum height of 80 m and a crown width of 170 m. The crown area is characterized by a complex morphology formed by a dense network of tension tracks and shear fissures in the weathered flysch formation of the Autapie Nappe forming a graben-like morphology. Counter-slopes with accumulated water are also observed. The tension cracks present a sub-vertical dip distributed along the circular shape of the crown. This spatial distribution is typical for failures in soft rocks (Cornforth 2005). The complex morphology is cut by three main persistent discontinuities D1, D2 and D3 visible over a distance of several hundred meters (Fig. 5).

The D1 fracture coincides with the direction of the Soleil Boeuf crest which represents the upper boundary of the landslide. D1 is characterized with a dip direction and a dip of 247°/42° ± 6°/4°. Because striations identified over the entire height of the crest present an orientation nearly parallel to the dip and dip direction of D1 (calcite recrystallization, pitch of S86°), the landslide is sliding above D1 without shearing component. The observed striations are a direct mechanical consequence of the sliding along D1.

The fractures D2 and D3 are characterized with dip directions and dips of $287^{\circ}/55^{\circ}$ $\pm 4^{\circ}/5^{\circ}$ and $166^{\circ}/44^{\circ} \pm 10^{\circ}/4^{\circ}$ respectively. D2 is located in the North-East of D1 and D3 is the conjugate fracture of D2. The landslide is sliding along D2 and D3 with a shearing component. The most active part of the landslide is actually constrained between these two discontinuities.

Laser scanning surveys

Acquisition of Airborne laser scanning (ALS) data

In order to determine the spatial extent of the main morpho-structural features, small-scale analysis of ALS has been carried out. The ALS survey was performed in July 2009 with the handheld airborne mapping system of the *Helimap* company) at a constant elevation of 300 m above the ground topography inducing a laser footprint at the ground surface of about 0.09 m (Vallet and Skaloud, 2004). The measurement device is composed of a GPS receiver (Topcon Legacy GGD with a record frequency of 5Hz), an inertia measurement unit (IMU, record frequency of 500 Hz) which provides the orientation of the laser beam in space and a scanner unit (Laser Riegl Q240i) configured to record last pulses of the ground surface with an acquisition frequency of $10'000 \text{ pts.s}^{-1}$. Table 1 summarizes the specification of the ALS survey. The orientation of the system is obtained in real-time with an accuracy estimated at 0.07 m. The maximum scanner range is about 850 m with an aperture angle of 60° . After vegetation filtering, an average point density of 4.1 pt.m^{-2} is obtained. A 0.5 m-mesh DEM from the ground surface elevation points has been generated with a Delaunay triangulation. The DEM was then used to calculate a shaded relief map and a difference map with a 10 m-mesh DEM interpolated from topographic contour lines before the landslide event (maximal elevation error of 10 m).

Acquisition of Terrestrial Laser Scanning (TLS) data

Displacement monitoring of the upper part of the landslide has been carried out by repeated TLS data acquisitions. The displacement monitoring device consists of a long-range terrestrial laser scan Optech ILRIS-3D based on the time-of-flight distance measurements using an infrared laser (Slob and Hack 2004). Mirrors inside the scanner allow the acquisition of a 40° wide and 40° high field of view in a single acquisition with about 2500 pts.s^{-1} with an effective range up to 800 m in field conditions (Table 1). Seven TLS datasets were acquired over the period 18 May 2008 to 27 May 2010 from the same base position (Fig. 5); the scanned area was orientated in the direction of the discontinuity D2 at a distance of 130 m from the base. At that distance the beam width diameter is estimated at 0.03 m. The discontinuity D1 (Soleil Boeuf crest) along the main scarp was systematically included in the scanning. The TLS datasets comprise 9 to 12 million points and the resulting mean point density on the ground surface is about 150 pts.m^{-2} at a distance of 130 m. Only the last return pulse is registered to maximize the number of points at the ground surface.

Vegetation filtering, co-registration and georeferencing of the sequential TLS datasets

The TLS datasets were processed and analyzed using the *Polyworks v.11* software (InnovMetric 2009). The vegetation filter consists of an automatic selection of the points localized beyond a minimum height relative to a low-resolution square-grid DEM surface computed on the sequential point clouds. In this study, the mesh size of the low resolution DEM was fixed at 0.5 m and the minimum height at 0.1 m. The filtering result is systematically controlled and manually refined. A co-registration procedure is then used

for aligning the sequential TLS point clouds in the same coordinate system. The co-registration applied in this study follows the methodology proposed by Teza et al. (2007) and Oppikofer et al. (2009). The sequential point clouds alignment is limited to a stable part in the image corresponding to the Soleil Boeuf crest. First a manual alignment procedure is used; then an automated Iterative Closest Point (ICP) algorithm is applied to minimize (least square method) the distance between the points belonging to the different sequential datasets. The co-registration procedure mainly depends on the accuracy of the ICP algorithm which is very sensitive to the roughness of the terrain and the accuracy of the measurements (Lee et al., 1999). Rough terrains yield higher reliability in the co-registration. Therefore a high point density was systematically acquired in this area to increase the topographic resolution ($\sim 0.3 \text{ pt.cm}^{-2}$). A good confidence is given to the co-registration quality because of the large size of the stable area of the image used for the co-registration (1000 m^2) in reference to the size of the moving area not introduced in the co-registration procedure (4300 m^2). The direct proximity of both areas in the datasets is also an advantage for an accurate co-registration.

For the absolute georeferencing, the ALS point clouds were used as a reference. The sequential TLS datasets were aligned as single point clouds on the ALS point cloud. The co-registration accuracy of the sequential point clouds is thus not affected by the georeferencing accuracy of the ALS point cloud, and is estimated at 0.07 m for the planar and vertical accuracy (Vallet and Skaloud, 2004).

308 *Accuracy of the TLS point clouds*

In order to assess the accuracy associated with the TLS measurements, repetitivity measurements were realized on a planar stratum of the main scarp, and corresponding to the black marls formation (9 m^2). This test zone is located approximately perpendicular to the laser beam direction at a distance of 120 m from the TLS base. The average point spacing was fixed at 0.15 m. The point cloud acquisition was compared to a reference (first acquisition, May 2008) using the ICP algorithm to calculate the misfit between each pair of points in both acquisitions theoretically located at the same position. The repetitivity analysis indicates that the measurement error of the TLS used in this study follows a normal distribution characterized with an average error μ of $1.0 \cdot 10^{-3} \text{ m}$ and a standard deviation σ of $1.2 \cdot 10^{-2} \text{ m}$. This calculated error is in agreement with the range of error given by the manufacturer.

The accuracy of co-registration procedure is given by the residual 3D misfit computed on the stable part of the TLS of the 18 May 2008 taken as the reference (Table 2). The same procedure is applied to assess the error of the absolute positioning relative to the ALS survey. The higher error in the absolute positioning is mainly related to the lower point density and accuracy of the ALS datasets providing less geomorphological details than the TLS survey (Table 2).

326 *Displacement characterization and quantification*

The displacements are calculated by comparing the TLS datasets with the reference. Two methods are used to quantify the displacements from the original point clouds. The first method is based on shortest distance comparison of point clouds. The second uses displacements of Specific Points (SPs)

The shortest distance (SD) comparison consists of computing for each point the distance to its nearest neighbor in the reference point cloud. This method is particularly useful to detect spatially distributed changes if the direction of movement is unknown and to define zones with different displacement directions (Oppikofer et al., 2009). In order to determine the vertical displacement affecting the upper part of the landslide, the SD is constrained to compute displacement only along the vertical direction (SDv) assuming a tolerance angle for the vertical direction of $\pm 10^\circ$. The results are therefore comparable to elevation changes computed with differential DEMs (Bitelli et al., 2004). The accuracy of the vertical displacement depends on two independent factors: (i) the co-registration

accuracy, and (ii) the computed distance D according to the tolerance angle which gives a maximal error E_{\max} ($E_{\max} = D \cdot \sin(10^\circ)$).

The observed movement of Specific Points (SPs) allows one to define the direction of displacements. In this study, natural SPs were chosen (Fig. 6). They consist of tree stumps recognizable in the unfiltered sequential point clouds. In order to assess the displacements of the SPs in the crown area, a method based on the roto-translation technique is used (Montserrat and Crosetto, 2008; Oppikofer et al., 2009). It takes into account both translation and rotation of individual objects and uses the very high density available in the point clouds. Eleven SPs were triangulated in the plane normal to the laser viewing direction in order to minimize the effect of shadow zones in the interpolation (Fig. 6). To calculate the true displacement field, the center points of the SPs in the first acquisition is determined by averaging the X, Y Z positions of the points forming the SPs. Then the triangulated SPs of the reference are aligned on their corresponding triangulated SPs in the sequential point clouds using the ICP algorithm implemented in *Polyworks* (Fig. 6). Finally, the displacement vectors of the SPs are given by the initial and the final position of the center points of the first acquisition. Because the SPs are very well defined, the error mainly depends on the co-registration accuracy of the sequential point clouds.

Seismic Tomography investigation

As the laser scanning data provide only information on the structure and the kinematics visible at the ground surface, additional geophysical data to obtain information in depth were acquired in order to better constrain the interpretation. Seismic tomography has proven to be an efficient technique to detect the contact between a landslide body (highly fractured) and a stable bedrock in the same type of geological setting as for La Valette (Jongmans et al., 2009; Grandjean et al., 2006; Grandjean et al., 2007). Three seismic tomography surveys of P and S-waves velocities (L1, L2, L3) have been carried out in the upper part of the landslide to characterize the seismic velocities (V_p , V_s) of the failed material and determine the extension in depth of the discontinuities D1 and D2 (Fig. 5). Two cross-sections were installed along the direction of the main slope and one cross-section was installed perpendicular to the previous line in order to cross the discontinuity D2.

The two longest devices are composed of 24 geophones (resonance frequency of 10 Hz) spaced each five meters in order to obtain a sufficient investigation depth for a large scale characterization of the landslide structure. The shortest devices, composed of 24 geophones spaced each two meters, bring information on the fracturing between the failed material and the bedrock. For the seismic source, one hundred grammes (100 gr) of pentrite were used for each shot. The processing of the first arrival travel time P wave was carried out with the Rayfract seismic tomography software based on the wavepath Eikonal traveltimes inversion algorithm (Schuster and Quintus-Bosz 1993). Figure 7a shows an example of the arrivals of the P waves and Surface waves. Dispersion of surface waves is closely related to the structure and properties of the landslide material and, in particular, to shear wave velocity. The vertical distribution of the shear wave velocity can be estimated on the basis of the dispersion analysis of different kinds of surface waves contained in the P-wave seismic records (Fig. 7b). The dispersion analysis results in the generation of a dispersion curve (frequency vs. phase velocity) for each geophone location. The shear waves velocity sections were therefore obtained using a spectral analysis of the surface waves (SASW method) with the surf96-CPS program (Hermann 1987) which allows one to analyse the dispersive character of surface waves (McMechan and Yedlin 1981) and to obtain a S-wave vertical velocity profile by 1D inversion of the dispersion curves (Tarantola 2005) (Fig. 7b). To derive a 2D section, the 1D shear-wave velocities inverted from each local dispersion curve are then interpolated along each seismic line.

In order to georeference the 2D tomographies, the location of each geophones was measured with a dGPS (horizontal and vertical accuracy of 0.04 m and 0.07 m). In each

profile, the geophone locations are then projected on a straight line in the local coordinate system calculated with a linear regression. The equations of the regression line allow one to allocate a 3D position in the local coordinate system for all nodes of the tomography.

Estimation of the volume of the failed mass

To estimate the volume of the failed mass, the SLBL (Sloping Local Base Level) method has been used. It is a generalization of the base level concept proposed by Mills (2003) and is defined as a surface above which the rocks are assumed to be erodible by landslides due to the absence of buttress (Golts and Rosenthal 1993; Jaboyedoff et al., 2004b). This method was successfully applied both on hard and soft rock slopes (Jaboyedoff et al., 2009; Travelletti et al., 2010). The SLBL method is used in this study by integrating the information from the seismic survey and the TLS interpretation.

The SLBL algorithm is based on an iterative routine that replaces the elevations of any mobile point of a digital elevation model (DEM) by the mean value of the altitude of its neighbours, allowing a certain tolerance. Points with an altitude (z_i) larger than the mean of their neighbours are replaced by the mean value of the two neighbours $(z_{i-1} + z_{i+1})/2$ or by this value plus a tolerance C . Explicitly, in 2D, the procedure can be formalized as follows (Jaboyedoff et al., 2004b):

$$\text{If } z_i > (z_{i-1} + z_{i+1})/2 \text{ then } z_i = (z_{i-1} + z_{i+1})/2 \quad (1)$$

The result is a straight line between z_{i-1} and z_{i+1} . The introduction of the tolerance value C leads to a second-degree curve:

$$\text{If } z_i > (z_{i-1} + z_{i+1})/2 - C \text{ then } z_i = (z_{i-1} + z_{i+1})/2 \pm C \quad (2)$$

The tolerance can produce holes between points, e.g with an altitude smaller than the altitude of the surroundings points. To avoid this, two additional conditions can be added to ensure that the new point has a higher altitude than the lowest of its neighbours:

$$\text{If } z_i > (z_{i-1} + z_{i+1})/2 - C \text{ and } (z_{i-1} + z_{i+1})/2 \pm C > z_{i-1} \text{ or } (z_{i-1} + z_{i+1})/2 \pm C > z_{i+1} \text{ then } z_i = (z_{i-1} + z_{i+1})/2 \pm C \quad (3)$$

If it is not the case, the altitude z_i of the point i is replaced by the lower altitude of its neighbours. The procedure is iterative, and is stopped once the change between two iterations is near a zero value and a failure surface nearly circular is obtained if the tolerance used is very different from zero. In order to take into account planar sliding along discontinuities, a small tolerance has to be used to fit the calculated failure surface on the observed discontinuities. In 3D, the procedure is similar, but the test is then performed using the highest and lowest values among the four closest neighbours. Some points must be fixed during the computation, to avoid the calculation of a flat topography. The discontinuities determined in this study from the field observations, the seismic tomographies and the TLS surveys are used to constrain the SLBL computations.

Results

Morpho-structural analysis

The combined analysis of the geological field observations, the shaded relief map and the differential DEM map allows one to propose a kinematic model of the landslide retrogression.

Although the highly dislocated flysch formation can be considered as a relatively soft rock, the shaded relief analysis with the differential DEM clearly demonstrates that, at small scale, the key factor controlling the failure geometry and the overall stability of the mass is not the flysch formation itself, but the spacing and the orientation of the discontinuities composed by D1, D2 and D3. Consequently, the upper part of the La Valette landslide can be divided in four terrain units (Fig. 8a). Since the triggering date in March 1982, the terrain unit 1 has been confined between the steep discontinuities D2 and D3 that constrained the landslide retrogression to the North-East. The failed mass is composed of coherent blocks (up to 50 m wide) which are sliding towards the main slope direction. These blocks form minor counter-slopes affected by multiple open tension cracks (up to 1 m in opening and in spacing) favoring water infiltration. The blocks are progressively dislocated and incorporated in the mudslide body downhill. The negative elevation difference developing along D1 indicates that the landslide retrogression to the North-East is limited by D1 which forces the retrogression to develop laterally to the North (Fig. 8b). As a consequence of the loss of buttress given by the terrain unit 1, the terrain units 2 and 3 are progressively destabilized. The terrain unit 4 (North-West side of D3) is characterized with a hummocky morphology indicating a lower destabilization of the slope due to the loss of buttress provided by the terrain unit 3 located downhill. At a smaller scale, the La Valette landslide appears to be included in a Deep-Seated Gravitational Slope Deformation (DSGSD) (Agliardi et al., 2001) which main scarp coincides with the extension of D1 to the North. In addition, the Soleil Boeuf crest presents the same morphology as before the triggering in 1982 when the scarp was located 200 m more to the South-West (Le Mignon, 2004). Therefore, the 1982 large failure is strongly suspected to be a reactivation of an older DSGSD along D1. Furthermore, the dip and dip direction of the Western side of the DSGSD main scarp ($166^{\circ}/38^{\circ} \pm 10^{\circ}/4^{\circ}$) is very similar to D3, suggesting that the old scarp face belongs to the same discontinuity set. Consequently, D3 can thus be a pre-existing fracture which is also reactivated. The difference in the fracturing degree on both sides of D2 clearly highlights the preferential extension of the landslide towards the North-West. On the South-East side of D2, no significant geomorphic evidence of current activity is observed except the extension of D1 which progressively disappears in the flysch formation to the South-East. Furthermore, no negative elevation difference is noticed in this area in reference to the vertical accuracy of the differential DEM (~ 10 m). The downhill limit of the negative elevation remarkably coincides with the tectonic discordance of the Autapie Nappe and the uphill limit corresponds to the spring area. The location of the triggering area of 1982 is clearly identified where the elevation difference (50 m) is the maximum.

Seismic tomography analysis

The tomographies of P and S-waves reveal a low velocity zone ($V_p < 900 \text{ m.s}^{-1}$, $V_s < 400 \text{ m.s}^{-1}$) in the terrain unit 1 affected by dense fracturing. The increase of P and S-waves velocity when one gets closer to the stable rock (fracture D1) gives a good confidence in the determination of the contact among the failed mass and the stable bedrock in depth (Fig. 9a, 9b). The velocities in the stable part composed of the flysch formation vary in the range 1200-2000 m.s^{-1} for the P-waves and 450-600 m.s^{-1} for the S-waves. These velocity values are slightly lower than those expected for similar rocks composed of conglomerate and sandstone with a low clay content (Gosar et al., 2001). They are explained by the highly dislocated texture of the flysch (BRGM 1974). Despite an important velocity contrast in V_s on both sides of D2, the extension of D2 in depth cannot be precisely determined on the tomographies because of insufficient velocity contrast in depth. Starting from the stable part, the iso-values of 1200 m.s^{-1} (V_p) and 450 m.s^{-1} (V_s) dip rapidly below the ground surface. This interface can be followed in all seismic tomographies between 12 and 15 m below the ground surface. It is difficult to determine the roughness of this interface knowing that the seismic tomographies very

often tend to produce artificial undulating surfaces because of the diffractions caused by small irregularities at the shallow surface of very heterogeneous media. Therefore, the interface can be modeled as a plane which is an acceptable assumption for a small-scale interpretation. The plane is adjusted in a least square sense on the tomography nodes at the transition between the velocities characterizing respectively the failed mass and the stable bedrock. A stronger weight is attributed to the V_p tomographies because the velocity contrasts are more important than in the V_s tomographies. The accuracy is estimated by adjusting different planes based on five different interpretations. The average orientation is thus characterized with a dip direction of $233^\circ \pm 8^\circ$ and a dip of $26^\circ \pm 4^\circ$ which is close to the average slope of the ground surface but lower than D1. Therefore this interface is not interpreted as the extension of D1 in depth, but as the limit of D4 between a highly fractured media and the less fractured bedrock in flysch. D4 could possibly correspond to an internal shear zone upon which a highly fractured rock is sliding in a dip-slope configuration.

Kinematics analysis

Displacements calculated from the TLS datasets between the period May 2008–May 2010 illustrate the landslide activity at the vicinity of D1, D2 and D3. The SDv computations on the point clouds indicate a maximum absolute elevation difference of 6.14 m between July 2008 and May 2010 (average error of 3.10^{-3} m with a standard deviation of 0.03 m) leading to an maximum vertical displacement rate of $3.07 \text{ m} \cdot \text{year}^{-1}$ along D1 and D2 of the top of the terrain unit 1 (Fig. 10). All the displacements in the terrain unit 1 are concentrated between D1 and D2 where tensions cracks are developing, thus explaining the low seismic velocities observed in this area (Fig. 9). The elevation differences allow one to distinguish three coherent blocks 1a, 1b and 1c belonging in the terrain unit 1 (Fig. 8a); these blocks are progressively separated by the opening of tension cracks and the sliding along D1 and D2. Uphill, the terrain unit 2 is also destabilized due to the loss of buttress provided by terrain unit 1. No displacement is detected on the South-East side of D2 with reference to the accuracy of the TLS datasets (less than 0.05 m). These observations are in agreement with the morpho-structural analysis described previously. The displacement amplitudes of the SPs are far larger than the accuracy of the TLS datasets, thus giving a good confidence in the measurements. The SPs displacements allow one to determine the true 3D displacement vectors characterized by an average velocity of about $4.12 \text{ m} \cdot \text{year}^{-1}$ (Fig. 11). The increase of the standard deviation of SPs displacements with the elapsed days between TLS acquisitions (Table 3) highlight the spatial heterogeneity of displacement in the top of the terrain unit 1 due to the progressive opening of tension cracks separating the blocks 1a, 1b and 1c (Fig. 10). On the opposite, the directions of the displacement vectors are constant in time and in space with an average dip direction and dip of $228^\circ/34^\circ (\pm 4^\circ/\pm 2^\circ)$ (Fig. 12). Consequently, the short term kinematics of the terrain unit 1 seems to be mainly controlled by planar failures along D1 and D4.

Concept for the failure mechanism

Because the upper part of the La Valette landslide is structurally controlled at small scale by planar sliding and wedge fracture configurations, a synthesis of the structural and kinematics analysis is done by the use of horizontal hemispherical projections (equal angle) (Richards et al., 1978; Hoek and Bray, 2004) (Fig. 12). The fracture sets identified in the terrain units 1, 2 and 4 are summarized in Table 4. Figure 13a presents the conceptual model of the failure mechanism interpreted from the integration of the ALS, TLS and seismic survey. From a kinematical point of view, D3 and D2 define a wedge geometry with an axis direction and dip of $215^\circ/30^\circ \pm 11^\circ/5^\circ$ and a maximum depth varying between 60 to 80 m with a back-crack represented by D1. Because the wedge axis does not ‘daylight’ in the

slope face, this geometry is precluded from a strict straight-forward wedge kinematic evaluation as a single homogeneous block (Hoek and Bray, 2004). In other words, the wedge cannot move without a buttress breakout. Therefore the wedge geometry can only constrain the landslide retrogression direction between D2 and D3 to the North. However a breakout interface cannot be totally excluded at the bottom of the scarp to explain the location of the source line and the subsidence along D1 in the terrain unit 1 (Fig. 13a). Downhill, the mudslide body is acting as a buttress for the upper part. Consequently, the progression of the mudslide allows the development of dip-slope failures and coherent blocks start sliding along D4 laterally delimited by D2 and D3. Because the dip direction and dip of the 2-years displacements vectors in the terrain unit 1 are located between the great circles of D1 and D4 (Fig. 12), the displacement vector components are likely related to a sliding along D1 and D4, thus leading to a bi-planar superimposed failure mechanism. In addition, the dip direction and dip of the displacements vectors are remarkably close to the intersection of the great circles of D2 and D3 which corresponds to the wedge axis orientation (Fig. 12). This observation consolidates the hypothesis of the predominant role of the wedge geometry on the long-term development of the landslide since its triggering date while the planar sliding explain the short-term landslide kinematics. D4 is probably not a pre-existing discontinuity and is likely related to a plastic deformation of the highly fractured flysch formation during the development of the dip-slope failure mechanism. The tension cracks observed at the ground surface are certainly connected to the shear zone D4 in depth, thus leading to a listric geometry which is usually observed in soft rocks and clay slopes.

Volume estimation with the SLBL method

To estimate the volume of the failed mass along D4 in the terrain unit 1, an interpolation is carried out using the SLBL method. The discontinuities D1 (North-East limit), D2 (South-East limit), D3 (North-West limit) and D4 (basal limit in depth) are used to constrain the calculation domain of the SLBL by assuming that D4 is continuous with a slightly curved geometry. The mechanical weak zone highlighted by the spring line at the lower limit of terrain unit 1 (Fig. 8; Fig. 13a) is used as the Southern limit for the SLBL calculation. The unstable volume is calculated using a 2 m grid DEM interpolated from the ALS data. This cell size is essentially used for computation stability and time computing purposes. A tolerance of -0.3 defining the degree of curvature of the SLBL is selected in such way that the SLBL surface fits at best the discontinuity D4. The result gives a slightly curved surface that flattens and daylight in the spring line A volume of 500'000 m³ is estimated (Fig. 13b). This volume represents the highly fractured mass mobilized by D4 which is currently loading the underlying mudslide body.

Discussion and Conclusion

In the La Valette landslide, the morpho-structural analysis and the displacement analysis indicated a structurally-controlled evolution of the landslide at small scale. The retrogression failure observed in the upper part of the La Valette landslide is an intermediate case study between landslide developed in soft and in strong rocks. In strong rocks, the relationship between pre-existing fractures and the failure mechanism has been widely observed and illustrated (Sauchyn et al., 1998; Agliardi et al., 2001; Jaboyedoff et al., 2009). In soft rocks, the failure mechanism is propagated through intact materials of uniform shear strength (Irfan, 1998). Therefore conventional stability analyses are not fully appropriate because of the influence of both the mechanics of the discontinuities and the mechanics of the deforming soil. Although this aspect is out of the scope of this study, it will need specific attention for a further slope failure modeling. In addition, in such slow-moving complex landslides in soft rocks, it is often difficult to determine the exact location of the failure surface. The deformation may occur at more than one level or in

different parts of the slope at different times (Cornforth, 2005). Therefore several additional failure surfaces not depicted in the conceptual model may be present in reality or may occur in the future. However, the proposed model is coherent with the ALS, TLS and seismic data and the field observations.

The upper part of the La Valette landslide is very probably a case of reactivation of an older landslide and is characterized with a succession of individual slides as it is often observed in large Deep-Seated Gravitational Slope Deformation (DSGSD) (Agliardi et al., 2001). A first slide occurs and, as a consequence of the movement of this mass, other adjacent masses starts to move thus allowing the retrogression of the landslide to the North. The opening of tension cracks in the crown area is evidence of the initiation of a progressive failure. However, the flysch formation may already have undergone some deformation before the discontinuities start to open. The failure may have started in the weak zone D4 and along the pre-existing fractures D1, D2 and D3. Furthermore, the pre-failure behavior of successive slides is probably a consequence of non-uniform stress and strain conditions which prevent the upper part to a catastrophic failure. In the same way, the dip of D4 extended by the SLBL calculation (internal sliding surface mobilizing 500'000 m³ of the landslide mass) is very close to the residual friction angle of the reworked flysch (30°) (Colat and Locat, 1993; Le Mignon, 2004; Fig. 13b). Therefore the stability limit is not reached simultaneously in the whole mass and it would be very unlikely that the unstable mass will fail in a single event. Because the wedge axis delimited by D2 and D3 does not 'daylight' in the slope face, the probability of a catastrophic failure is considerably reduced to a progressive release of material through shallow translational failure mechanisms controlled by D1 and D4. However the existence of breakout interfaces at the bottom of the main scarp cannot be totally excluded (Fig. 13a). Stresses would then be transferred by loading to the mudslide body acting as a reinforced buttress since the set-up of the drainage system in the middle part of the slope and the decrease of the mudslide velocity. The stress release occurs over an extended period due to the continuous sliding of the mudslide body (~1 m.year⁻¹). However, this buttress can become over-stressed if the activity of the upper part increases, thus potentially leading to a sudden acceleration of the mudslide or the development of an upper internal failure in the mudslide body. If the stress increment becomes excessive, the amount of deformation becomes deviated in the shallow part of the slope, thus leading to an increase of the slope inclination favoring shallow failures. Sudden releases of small volumes and fluidization of the mass at the vicinity of the spring line have been observed in the past and more recently in Spring 2009 when about 3000 m³ of reworked flysch suddenly mobilized in a mudflow over a distance of 250 meters. A development of the mudslide in areas where the buttress is less strong typically in the borders of the mudslide through lateral spreading is also possible. As a consequence of the important activity of the upper part, the lower mudslide part has to evolve differently than in the past according to the drainage works installed further downhill. The transition between the main scarp and the mudslide body constitutes a key zone controlling the overall landslide behavior because that part is susceptible to be over-stressed. Groundwater conditions of the upper part still need to be assessed in detail for a better understanding of the failure mechanisms. Hydro-mechanical modelling in progress will also help to better understand the failure mechanism.

To conclude, the efficiency of combining ground-based (LiDAR TLS, seismic tomography) and airborne-based (LiDAR ALS) geophysical information to characterize the landslide structure is demonstrated by the agreement observed between geological field observations, morpho-structural modeling and kinematics analysis. The advantage of combining different methods is to propose an interpretation adapted to the scale of the landslide which is not possible when only local (e.g. punctual) measurements are used. TLS data provide high resolution point clouds of the topography for large scale analysis which complements ALS data which are more suitable for smaller scale analysis. The seismic tomography survey provides spatially-distributed information on the geometry of the fractures in depth. The integration and the interpretation of this multi-source data allow one to propose possible landslide evolution scenarios. Furthermore, this study

demonstrated that in soft rocks (e.g flysch formations), the morpho-structure information derived from field observations and DEMs analysis does not fully reflect the internal structure of the slope without complementary information on the kinematics and on the internal structure provided with ground-based surveys. The proposed multi-technique approach can be applied to different types of landslides. A simple plot of the displacement vector in a stereonet with the observed discontinuity orientations can highlight structurally controlled landslides. This approach has been illustrated in the monitoring of strong rock-slope. Because multi-source data have heterogeneous qualities and different spatial resolutions, a major difficulty consists in the extraction of relevant information and in their integration in a coherent framework. Data georeferencing and re-interpretation are among the most important steps needed to detect inconsistencies among multi-source data (Caumon et al., 2009; Travelletti and Malet, 2011). A future challenge to improve the proposed methodology relies on coupling of 3D Geographic Information Systems (data storage and management) with 3D geometrical modeling packages allowing quick re-interpretation of the conceptual model of the slope.

Acknowledgements

This work was supported by the European Commission under the Marie Curie Contract ‘*Mountain Risks: from prediction to management and governance*’ (FP6, MCRTN-035798; 2007-2010), and by the French Ministry of Research within the project ‘*SISCA: Système Intégré de Surveillance de Crises de glissements de terrain argileux*’ (Contract ANR Risk-Nat, 2009-2012). The authors would like to acknowledge Mr. Georges Guiter and Mr. Michel Peyron from (RTM - *Restauration des Terrains en Montagne*, Office of Barcelonnette) for their assistance and discussion in the field. The authors are also grateful to Mr. Grzegorz Skupinski (University of Strasbourg) for his support in the acquisition of the Terrestrial Laser Scanning data. The authors are also grateful to two anonymous reviewers for their constructive comments.

References

- Agliardi F, Crosta G, Zanchi A 2001 Structural constraints on deep-seated slope deformation kinematics. *Engineering Geology* 59: 83–102
- Bitelli G, Dubbini M, Zanutta A 2004 Terrestrial laser scanning and digital photogrammetry techniques to monitor landslide bodies. In: *Proceedings of the XXth ISPRS Congress ‘Geo-Imagery Bridging Continents’*, XXXV, Part B5, Istanbul, Turkey, 12–23 July 2004, ISPRS, pp 246–251
- BRGM (Bureau des Recherches Géologiques et Minières) 1974. Carte et notice géologique de Barcelonnette au 1:50.000è. XXXV-39. Orléans, France, 38 p
- Caris JPT, van Asch ThWJ 1991 Geophysical, geotechnical and hydrological investigations of a small landslide in the French Alps. *Engineering Geology* 31(3–4): 249–276
- Casson B, Delacourt C, Allemand P 2005 Contribution of multi-temporal sensing images to characterize landslide slip surface – Application to the La Clapière landslide (France). *Natural Hazards and Earth System Sciences* 5: 425–437
- Caumon G, Collon-Drouaillet P, Le Carlier de Veslud C, Sausse J, Visuer S 2009 Teacher’s aide: 3D modeling of geological structures. *Mathematical Geosciences* 41(9): 927–945.
- Colas G, Locat J 1993 Glissement et coulée de La Valette dans les Alpes-de-Haute-Provence. Présentation générale et modélisation de la coulée. *Bulletin de Liaison des Laboratoires des Ponts et Chaussées* 187: 19–28
- Cornforth DH 2005 Landslides in practice: investigation, analysis and remedial/preventative options in soils. Wiley, USA, 625p
- Cruden DM 1976 Major slides in the Rockies. *Canadian Geotechnical Journal* 13: 8–20

- Cruden DM, Martin CD 2004 Before the Frank Slide: preparatory & triggering causes from maps and photographs. In: Proceedings of the 57th Canadian Geotechnical Conference, GeoQuébec 2004
- Crosta GB, Agliardi F 2003 Failure forecast for large rock slides by surface displacement measurements. Canadian Geotechnical Journal 40: 176–191
- Déprez A, Malet J-P, Masson F, Ulrich P 2010 (submitted) Continuous monitoring and near-real time processing of GPS observations for landslide analysis: a methodological framework. Engineering Geology, 16p. (submitted)
- Dupont M, Taluy P 2000 Hydrogéologie du glissement de La Valette (avec carte au 1:5000^e des venues d'eau). Internal Report, Université de Savoie, Chambéry, France, 45p http://eost.u-strasbg.fr/omiv/Publications_la_valette.html
- Eberhardt E, Thuro K, Luginbuehl M 2005 Slope instability mechanisms in dipping interbedded conglomerates and weathered marls – the 1999 Rufi landslide, Switzerland. Engineering Geology 77: 35–56
- Evin M 1992 Prospection sismique en partie basse de la coulée de La Valette. Internal Report, RTM – Restauration des Terrains en Montagne, Barcelonnette, France http://eost.u-strasbg.fr/omiv/Publications_la_valette.html
- Feng QH, Röshoff K 2004 In-situ mapping and documentation of rock faces using a full-coverage 3-D laser scanning technique. International Journal of Rock Mechanics and Mining Sciences 41: 139–144
- Golts S, Rosenthal E 1993 A morphotectonic map of the northern Arava in Israel derived from isobase lines. Geomorphology 7: 305–315
- Gosar A, Stopar R, Car M, Mucciarelli M 2001 The earthquake on 12 April 1998 in the Krn mountains (Slovenia): ground-motion amplification study using microtremors and modelling based on geophysical data. Journal of Applied Geophysics 47: 153–167.
- Grandjean G, Pennetier C, Bitri A, Méric O, Malet JP 2006 Caractérisation de la structure interne et de l'état hydrique de glissements argilo-marneux par tomographie géophysique: l'exemple du glissement-coulée de Super-Sauze. Comptes Rendus Géosciences 338(9): 587–595
- Grandjean G, Malet J.-P., Bitri A, Méric O 2007 Geophysical data fusion by fuzzy logic for imaging the mechanical behaviour of mudslides. Bulletin de la Société Géologique de France, 178(2): 127–136
- Hermann RB 1987 Computer programs in seismology. Saint-Louis University, Saint-Louis, MO, USA, 317p
- Hoek E, Bray JW 2004 Rock Slope Engineering. Civil and Mining. Fourth Edition. Institute of Mining and Metallurgy London, UK, 456p
- InnovMetric, 2009 PolyWorks User's Manual - 3-D scanner and 3-D digitizer software from InnovMetric Software Inc., <http://www.innovmetric.com/>
- International Society for Rock Mechanics (ISRM) 1981 Rock Characterization, Testing and Monitoring; ISRM Suggested Method. Pergamon Press, Oxford, UK.
- Irfan TY 1998 Structurally controlled landslides in saprolitic soils in Hong Kong. Journal of Geotechnical and Geological Engineering 16: 215–238
- Jaboyedoff M, Ornstein P, Rouiller JD 2004a Design of a geodetic database and associated tools for monitoring rock-slope movements: the example of the top of Randa rockfall scar. Natural Hazards and Earth System Sciences 4: 187–196
- Jaboyedoff M, Baillifard F, Couture R, Locat J, Locat P 2004b New insight of geomorphology and landslide prone area detection using DEM. In: Lacerda WA, Ehrlich M, Fontoura AB, Sayo A (eds.), Landslides evaluation and stabilization, Balkema, Rotterdam, pp 199–205
- Jaboyedoff M, Couture R, Locat P 2009 Structural analysis of Turtle Mountain (Alberta) using digital elevation model: toward a progressive failure. Geomorphology 103: 6–16
- Jongmans D, Garambois S 2007 Geophysical investigation of landslides: a review. Bulletin de la Société Géologique de France 178(2): 101–112
- Jongmans D, Bièvre G, Renalier F, Schwartz S, Beaurez N, Orengo Y 2009 Geophysical investigation of a large landslide in glaciolacustrine clays in the Trièves area (French Alps). Engineering Geology 109: 45–56
- Lee BU, Kim CM, Park RH, Nurre JH, Corner BR 1999 Error sensitivity of rotation angles in the ICP algorithm. SPIE Proceedings Series A., 3640: 146–156
- Le Mignon G 2004 Analyse de scénarios de mouvements de versants de type glissement-coulées. Application à la région de Barcelonnette (Alpes-de-Haute-Provence, France). PhD Thesis, Ecole Nationale des Ponts et Chaussées, Paris, France, 210 p
- Le Mignon G, Cojean R 2002 Rôle de l'eau dans la remobilisation de glissements-coulées (Barcelonnette, France). In : Wagner P, Rybar J, Stemberk J (eds). Proceedings of the first European Conference on Landslides, Prague, Czech Republic. pp 239-244.

765 LePrince S, Berthier E, Ayoub F, Delacourt C, Avouac J-P 2008 Monitoring Earth earth Surface
 766 surface Dynamics dynamics With with Optical Imagery. *Eos*: 89, 1-5.
 767 Leroueil S 2001 Natural slopes and cuts: movement and failure mechanisms. *Geotechnique* 51:
 768 197–243
 769 McMechan GA, Yedlin MJ 1981 Analysis of dispersive waves by wave field transformation.
 770 *Geophysics* 46: 869–874
 771 Méric O, Garambois S, Cadet H, Malet JP, Guéguen P, Jongmans D 2007 Seismic noise based
 772 methods for soil landslide characterization, *Bulletin de la Société Géologique de France*,
 773 178(2): 137-148.
 774 Mills HH 2003 Inferring erosional resistance of bedrock units in the East Tennessee mountains
 775 from digital elevation data. *Geomorphology* 55: 263–281
 776 Monserrat O, Crosetto M 2008 Deformation measurement using terrestrial laser scanning data and
 777 least squares 3-D surface matching. *ISPRS Journal of Photogrammetry* 63: 142–154
 778 Oppikofer T, Jaboyedoff M, Kreusen HR 2008 Collapse at the Eastern Eiger flank in the Swiss
 779 Alps. *Nature Geoscience* 8: 531–535
 780 Oppikofer T, Jaboyedoff M, Blikra LH, Derron MH, Metzger R 2009 Characterization and
 781 monitoring of the Aknes rockslide using terrestrial laser scanning. *Natural Hazards and Earth*
 782 *System Science* 9: 1003–1019
 783 Prokop A, Panholzer H 2009. Assessing the capability of terrestrial laser scanning for monitoring
 784 slow moving landslides. *Natural Hazards and Earth System Sciences* 9: 1921–1928
 785 Richards LR, Leg GMM, Whittle RA 1978 Appraisal of stability conditions in rock slopes. In:
 786 Bell FG (ed): *Foundation engineering in difficult ground*. Newnes-Butterworths, London, pp.
 787 449–512
 788 Rosser NJ, Petley DN, Dunning SA, Lim M, Ball S 2007 The surface expression of strain
 789 accumulation in failing rock masses. In: Eberhardt E, Stead D, Morrison T (eds): *Rock*
 790 *mechanics: meeting Society's challenges and demands*. Proceedings of the 1st Canada–U.S.
 791 *Rock Mechanics Symposium*, Vancouver, Canada, 27–31 May 2007, Taylor & Francis,
 792 pp. 113–120
 793 Sartori M, Baillifard F, Jaboyedoff M, Rouiller JD 2003 Kinematic of the 1991 Randa rockfall
 794 (Valais, Switzerland). *Natural Hazards and Earth System Sciences* 3: 423–433
 795 Sauchyn DJ, Cruden DM, Hu HQ 1998 Structural control of the morphometry of open rock basins,
 796 Kananaskis region, southwestern Alberta. *Geomorphology* 22: 313–324
 797 Schuster GT, Quintus-Bosz A 1993 Wavepath eikonal traveltime inversion: theory. *Geophysics*
 798 58: 1314–1337
 799 Squarzoni C, Delacourt C, Allemand P 2003 Nine years of spatial and temporal evolution of the
 800 La Valette landslide observed by SAR interferometry. *Engineering Geology* 68: 53– 66.
 801 Squarzoni C, Delacourt C, Allemand P 2005 Differential single-frequency GPS monitoring of the
 802 La Valette landslide (French Alps). *Engineering Geology* 79: 215– 229.
 803 Slob S, Hack R 2004 3D Terrestrial Laser Scanning as a new field measurements and monitoring
 804 technique. In: Hack R, Azzam R., Charlier R. (eds): *Engineering geology for infrastructure*
 805 *planning in Europe. A European perspective*. Lecture Note in Earth Sciences. Springer, Berlin-
 806 Heidelberg, pp 179–190
 807 Tarantola A 2005 Inverse problem theory and methods for model parameter estimation. SIAM –
 808 Society for Industrial and Applied Mathematics, Philadelphia, U.S.A, 342 p
 809 Teza G, Galgaro A, Zaltron N, Genevois R 2007 Terrestrial laser scanner to detect landslide
 810 displacement fields: a new approach. *International Journal of Remote Sensing* 28: 3425–3446
 811 Travelletti J, Oppikofer T, Delacourt C, Malet J-P, Jaboyedoff M 2008 Monitoring landslides
 812 displacements during a controlled rain experiment using a long-range terrestrial laser scanning
 813 (TLS). In: *ISPRS - The International Archives of the Photogrammetry, Remote Sensing and*
 814 *Spatial Information Sciences*. Vol. XXXVII. Part B5, pp. 485–490
 815 Travelletti J, Malet J-P, Hibert C, Grandjean G 2009 Integration of geomorphological, geophysical
 816 and geotechnical data to define the 3D morpho-structure of the La Valette mudslide (Ubaye
 817 Valley, French Alps). In: Malet J-P, Rémaitre A, Boogard T. (eds) *Proceedings of the*
 818 *International Conference on Landslide Processes: from geomorphologic mapping to dynamic*
 819 *modelling*, Strasbourg, CERG Editions, pp 203-208
 820 Travelletti J, Demand J, Jaboyedoff M, Marillier F 2010 Mass movement characterization using a
 821 reflection and refraction seismic survey with the sloping local base level concept.
 822 *Geomorphology* 116: 1–10
 823 Travelletti J, Malet J-P (2011) Characterization of the 3D geometry of flow-like landslides: a
 824 methodology based on the integration of heterogeneous multi-source data. *Engineering*
 825 *Geology*. doi.org/10.1016/j.enggeo.2011.05.003

826 Travelletti, J, Delacourt, C, Allemand, P, Malet, J-P, Schmittbuhl, J, Toussaint, R, Bastard, M
827 2011 (in press). Correlation of multi-temporal ground-based images for landslide monitoring:
828 application, potential and limitations. ISPRS Journal of Photogrammetry and Remote
829 Sensing, 17p (accepted, in press).
830 Vallet J, Skaloud J 2004 Development and experiences with a fully-digital handheld mapping
831 system operated from a helicopter. In: The International Archives of the Photogrammetry,
832 Remote Sensing and Spatial Information Sciences, Istanbul, Vol. XXXV, Part B5.

Tables

Table 1 Characteristics of the LiDAR datasets

Characteristics of the laser scanning systems	ALS	TLS
Scanner type	Riegl VQ480	Optech ILRIS-3D
Distance measurement technique	Time-of-flight	Time-of-flight
Wavelength (nm)	1500	1500
Field of view (in width and height) (°)	60	40
Laser spot diameter at 100 m (cm)	~3	~3
Frequency of measurements (Hz)	10'000	2'500
Characteristics of the field acquisitions		
Scan distance (m)	~ 300	~130
Pulse mode	Last echos	Last echos
GPS frequency (Hz)	5	Scan from a base position
Point density after vegetation filtering (pt.m ⁻²)		
Average	4.1	154.8
Standard deviation	4.3	140.6

Table 2 Average error μ and standard deviation σ of the relative and absolute co-registration of the TLS datasets

	Relative positioning error		Absolute positioning error	
	μ (m)	σ (m)	μ (m)	σ (m)
18 May 08	-	-	0.04	0.07
25 July 08	0.00	0.03	0.06	0.08
10 May 09	0.00	0.03	0.02	0.07
12 July 09	0.00	0.02	0.04	0.09
08 Oct. 09	0.00	0.03	0.00	0.07
26 Apr.10	0.00	0.02	0.01	0.07
27 May 10	0.00	0.03	0.01	0.07

Table 3 Average μ and standard deviation σ of the SPs displacements

	Elapsed days	μ (m)	σ (m)
18 May 08 - 25 July 08	68	1.69	0.07
25 July 08 -10 May 09	289	3.3	0.34
10 May 09 - 12 July 09	63	0.52	0.05
12 July 09 - 08 Oct. 09	88	0.39	0.09
08 Oct. 09 - 26 Apr.10	200	1.93	0.17
26 Apr. 10 - 27 May 10	31	0.34	0.05

Table 4 Characteristics of the fracture sets identified in the terrain units 1, 2 and 4 of the La Valette landslide

	Number of observations	Dip direction (°)	Dip (°)
D1	52	247	42
D2	11	287	55
D3	77	166	44
D4	5	233	26

Figure captions

Fig. 1. Geomorphological setting of the La Valette landslide on the South-facing slope of the Barcelonnette basin. a) General view of the landslide to the North East. b) View of the main scarp and the crown areas; the dashed line delineates the area investigated by TLS and seismic tomographies. The displacement profiles measured by the “Restauration des Terrains de Montagne, RTM” office to monitor the retrogression of the crown are also indicated.

Fig. 2. Geological setting of the La Valette landslide. a) Extract of the regional geological map at 1:50.000 with the topography before the landslide event (adapted from BRGM, 1974) and schematic cross-section detailing the hydro-geological setting of the slope before the failure of 1982 (adapted from Colat and Locat, 2003). The interval between elevation contour lines is 20 m b) Photographs of the spring line at an elevation of ca. 1880 m along a possible weak zone above the tectonic discordance near the North West boundary and the Rocher Blanc location.

Fig. 3. Development of the La Valette scarp since 1974 (before the failure) to 2009 from the analysis of aerial orthophotograph. From 1982 to 2009 a scarp regression of 200 m towards the North East is observed.

Fig. 4. Displacement monitoring of some profiles along the crown (monitoring carried out by the “Restauration des Terrains de Montagne, RTM” office). The monitoring indicates an acceleration of the displacement since 2000. The displacement profiles measured by RTM are also indicated on the orthophotograph of 2009..

Fig. 5. Photographs of the crown area presenting three major discontinuities D1, D2 and D3 and the associated stereonet (equal angle, lower hemisphere). Striations are observed on D1. The location of the terrestrial laser scanning (yellow square) and the seismic profiles (L1, L2 and L3) are also indicated.

Fig. 6. Location of the eleven SPs in the crown area used to calculate the displacements. The SPs of the first acquisition are aligned on their corresponding displaced SPs for each acquisition date. The displacement of the center point of each SP of the first acquisition is used to determine the displacement vector. The average misfit between the SP of the first acquisition and the corresponding SP is estimated at ca. 0.01 m.

Fig. 7. Example of seismic tomography data from the profile L2 (see location in Figure 5). a) Example of recordings of the P-waves and Surface-waves arrival time. The first arrivals of the P-waves are used for the inversion of the P-wave velocity tomography. A spectral analysis of the surface waves (SASW) is realized to measure the surface wave dispersion curve and invert the corresponding shear wave velocity b) Example of the analysis of the dispersive character of surface waves for the 1D inversion of a vertical profile of shear wave velocity. The phase velocity represents the velocity of individual wave propagation in the media according to its wavelength and frequency (Park et al. 1998). The relative good determination of the dispersion curve (dashed line) gives confidence on the inverted shear-wave velocity profile.

Fig. 8. Morpho-structural maps derived from the interpretation of an Airbone Laser Scanning (ALS) survey. a) Major discontinuities and sub-units identified in the scarp and in the crown areas. b) Differential DEM highlighting the retrogression direction of the landslide for the period 1960-2009 constrained by the discontinuity D2 and D3.

Fig. 9. 3D view of the seismic tomographies with their location in the crown area a) P-wave velocity tomography. b) S-wave velocity tomography. A velocity contrast at about 12 m deep highlights the presence of the discontinuity D4 interpreted as an internal sliding surface.

Fig. 10. TLS point cloud comparisons according to the reference date of 18 May 2008. The displacements are calculated with the shortest distance comparison in the vertical direction. A negative value means that the point elevation is lower than the point of the reference. Several blocks are clearly individualized through time. The blocks 1a, 1b and 1c belong to the sub-unit 1. The block 2 belongs to the sub-unit 2. The displacement vectors of the SPs are also indicated.

Fig. 11. Cumulated displacements of the SPs calculated with the roto-translation technique.

Fig. 12. Stereonet (equal angle, lower hemisphere) of the major discontinuities observed in the scarp and in the crown areas. The direction of displacement located between the great circles of D4 and D1 near the intersection of D2 and D3 strongly suggest that the upper part of the La Valette landslide is structurally-controlled by planar failure confined within a wedge geometry.

Fig. 13. Conceptual geological model of development of the upper part of the La Valette landslide. a) Proposed concept of the failure mechanism affecting the scarp and the crown areas. The morpho-structural and the kinematics analyses highlight a planar failure mechanism along D1 and D4 confined in a wedge geometry delimited by D2 and D3. The location of the cross-section is shown in Fig. 13b. b) 3D view of the discontinuity D4 extended with the SLBL computation. The ground topography above D4 has been removed.

Figure 1
[Click here to download high resolution image](#)

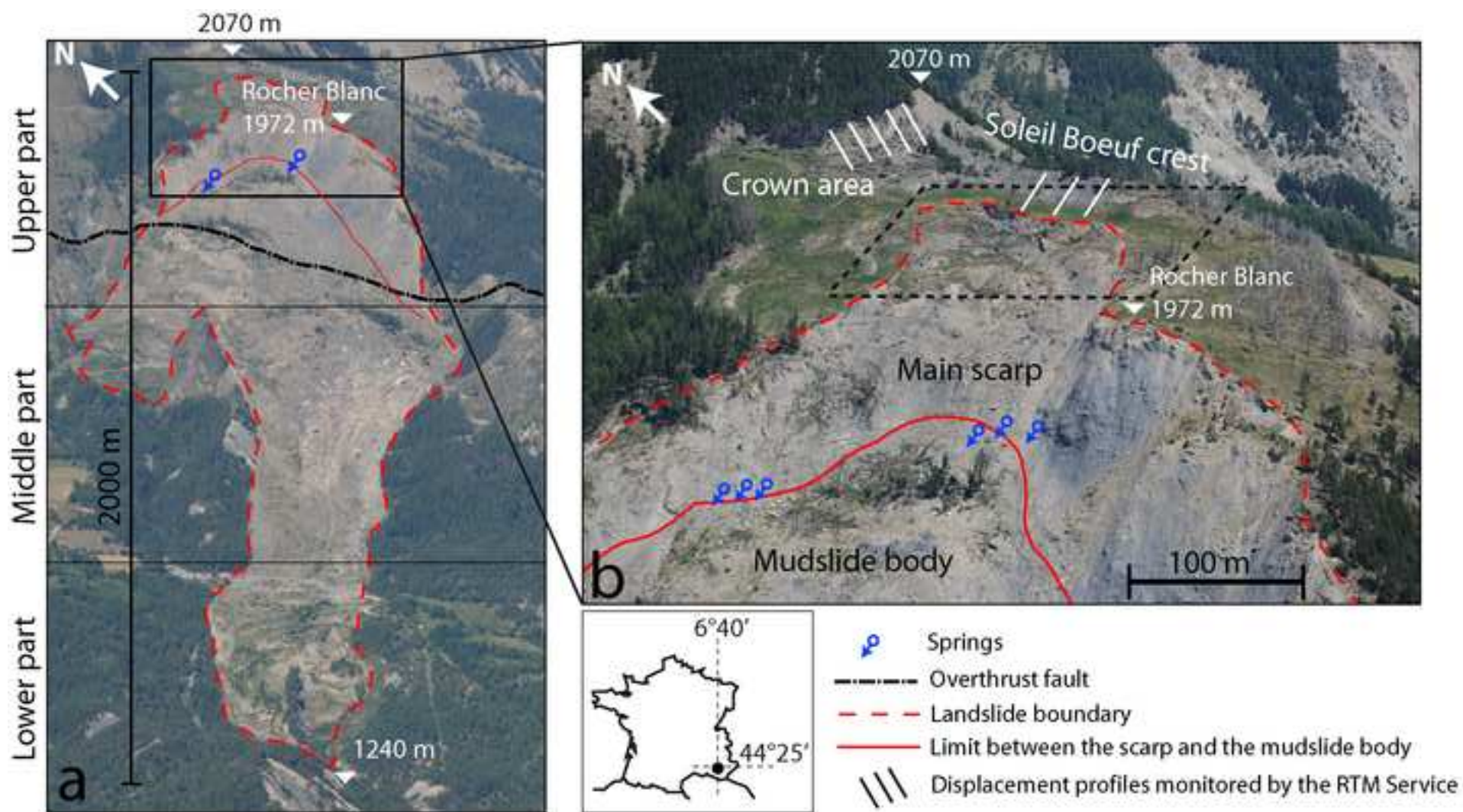


Figure 2
[Click here to download high resolution image](#)

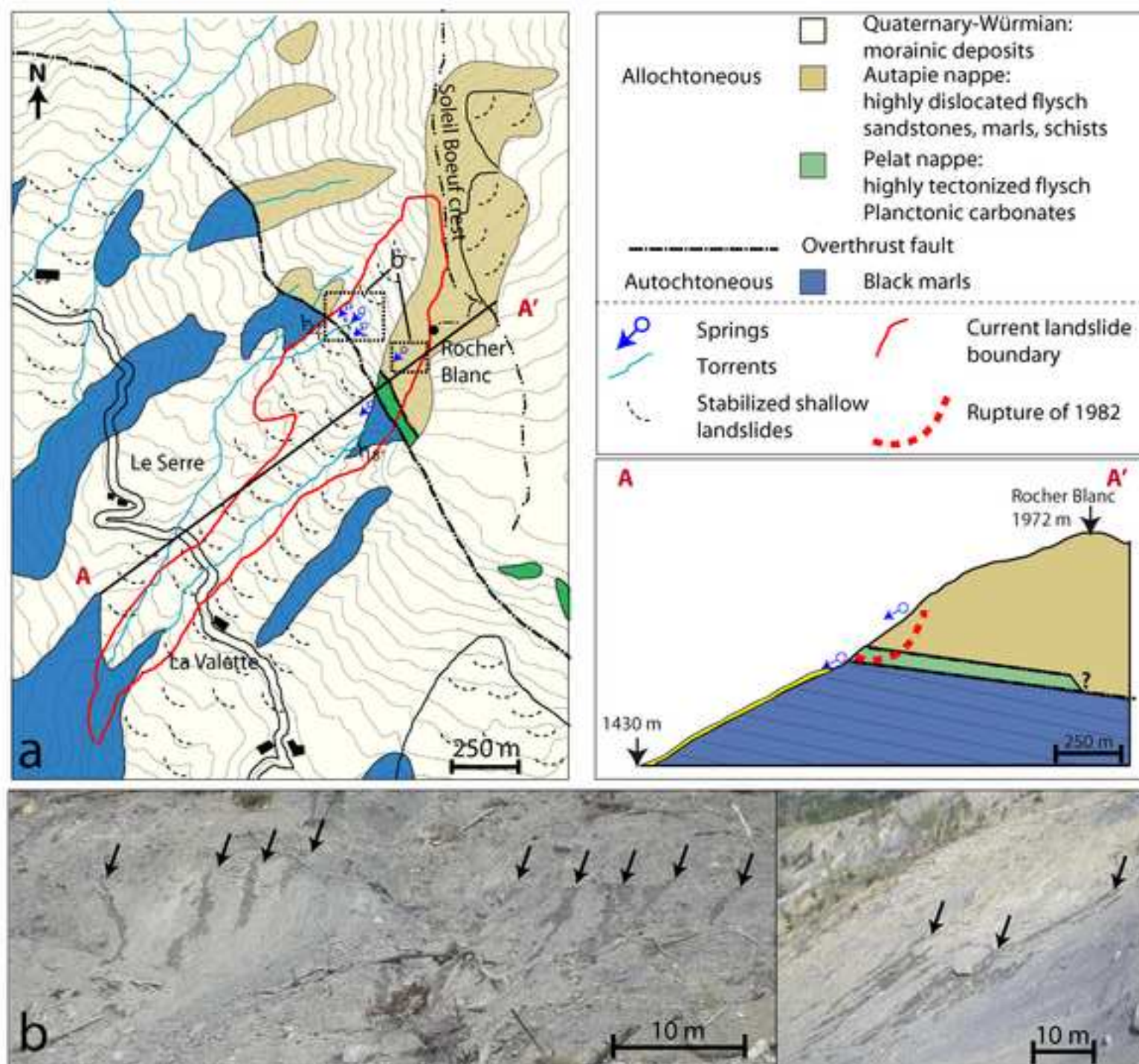
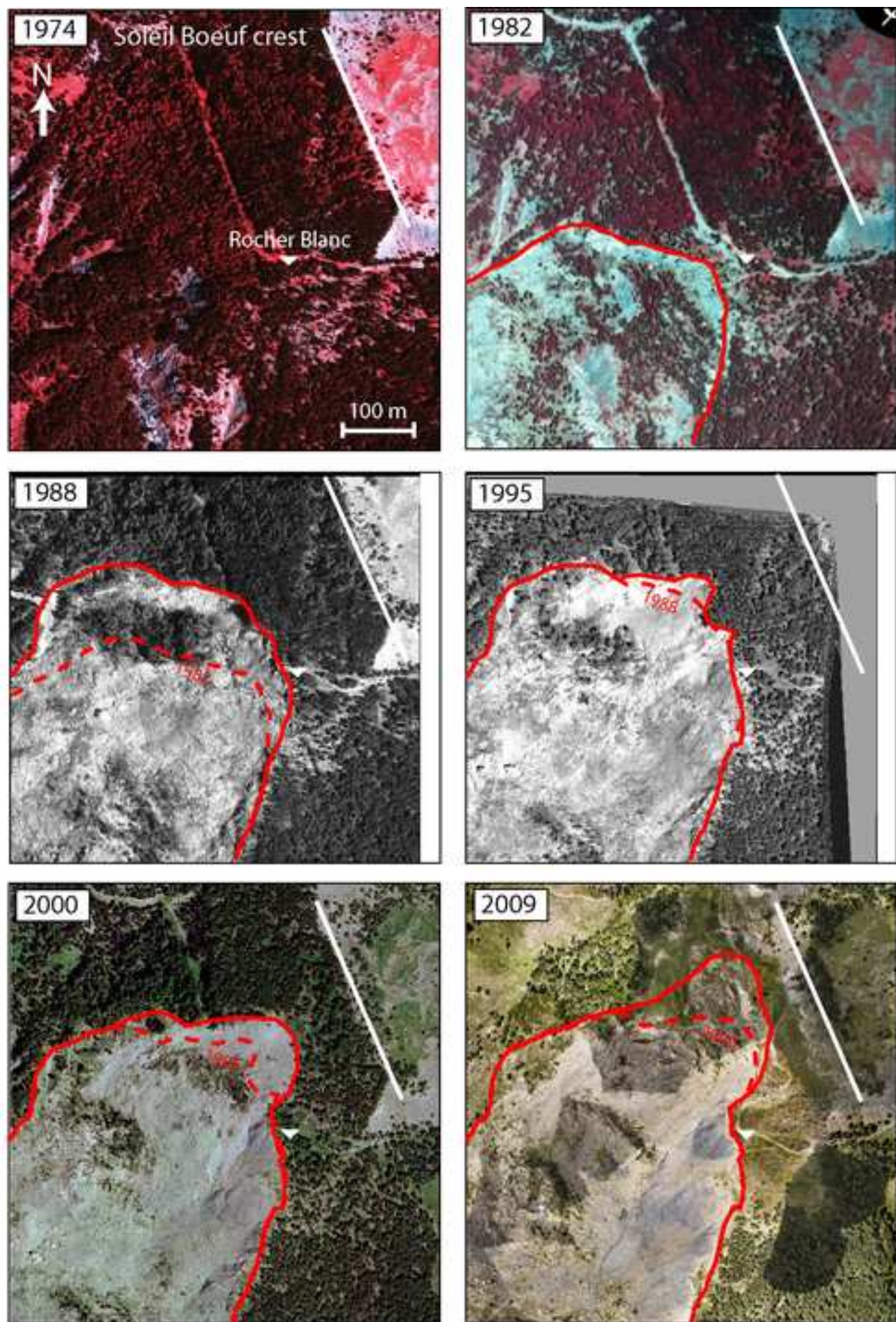


Figure 3
[Click here to download high resolution image](#)



[Click here to download high resolution image](#)



Figure 5

[Click here to download high resolution image](#)

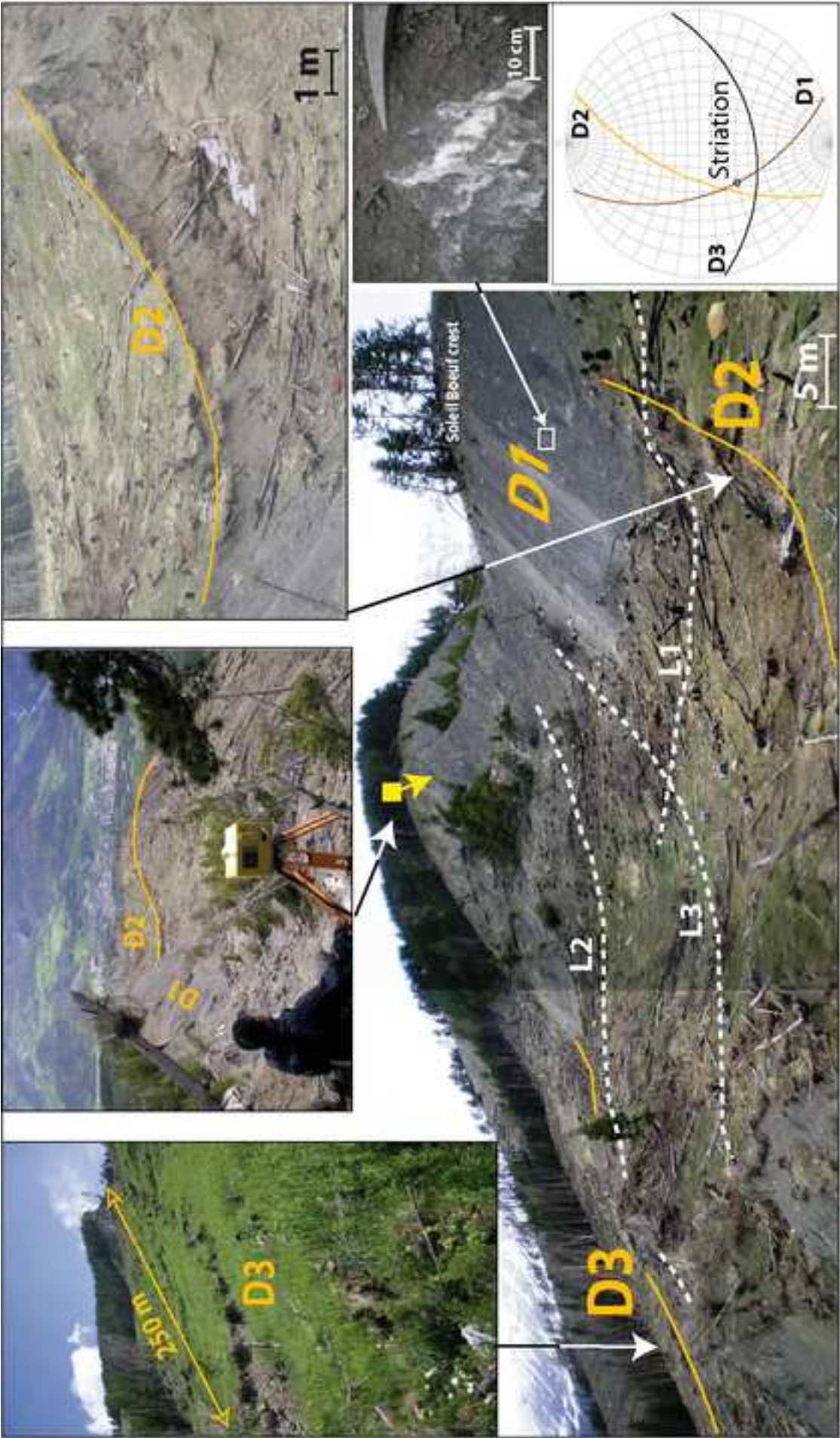


Figure 6
[Click here to download high resolution image](#)

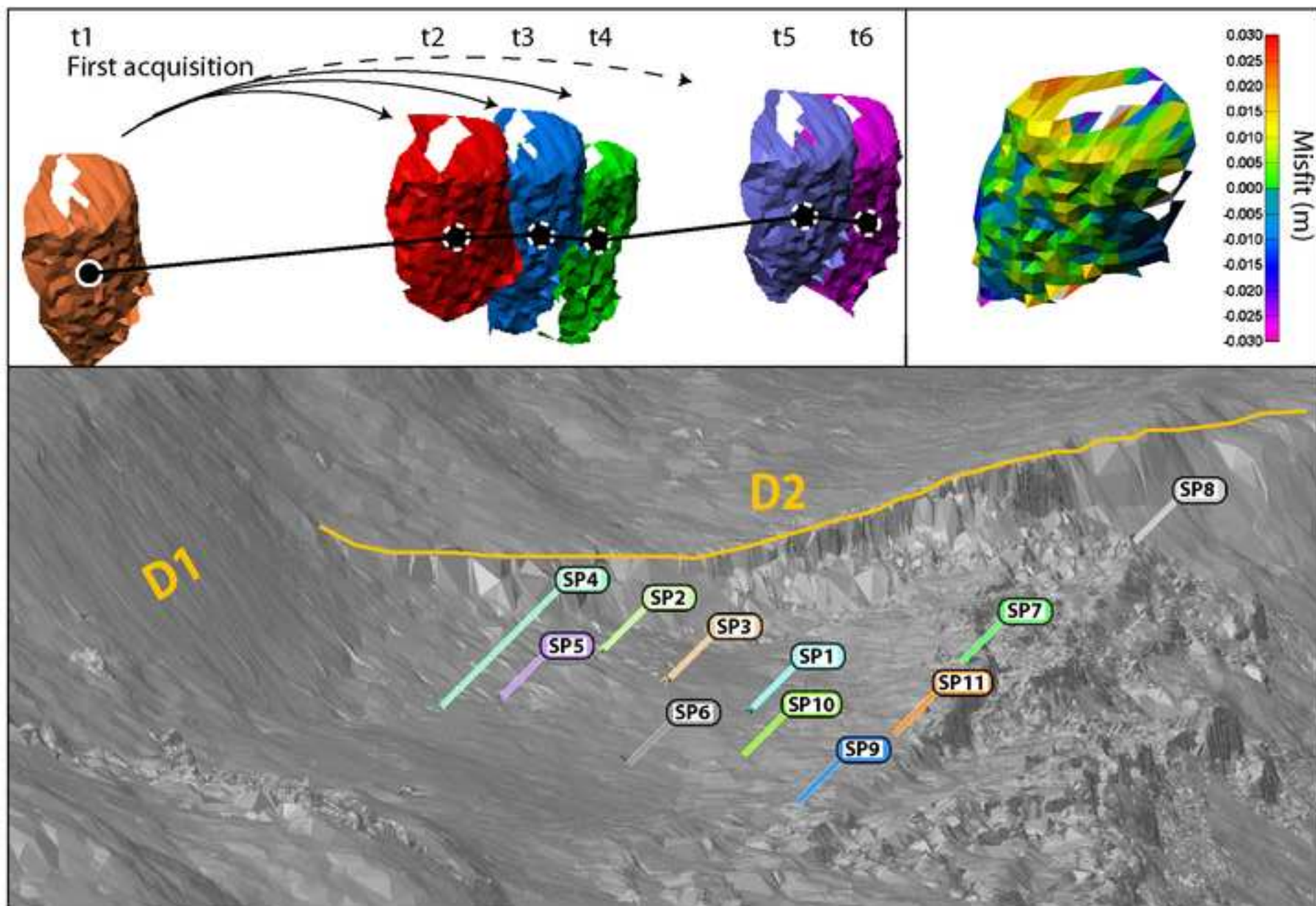


Figure 7
[Click here to download high resolution image](#)

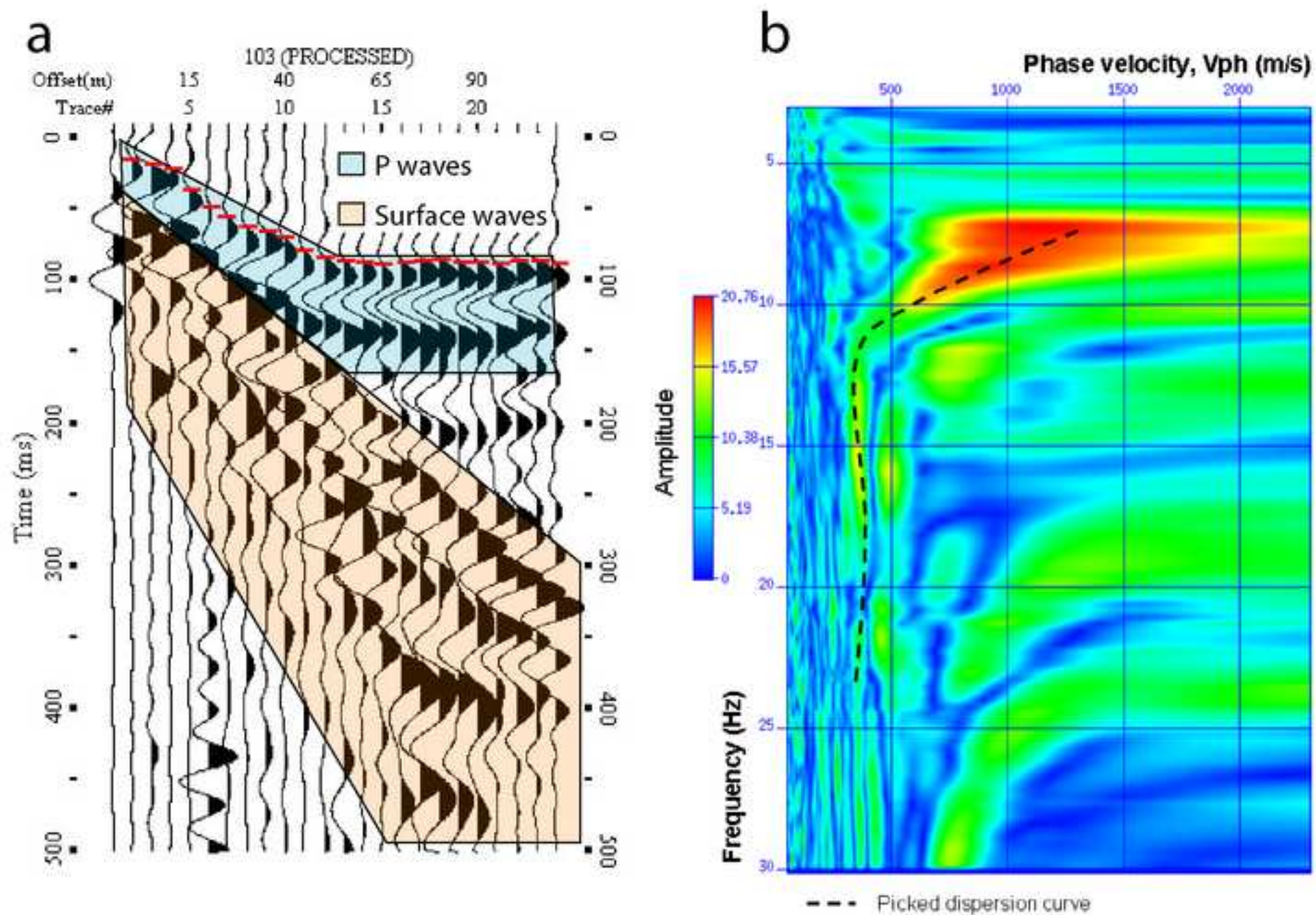


Figure 8
[Click here to download high resolution image](#)

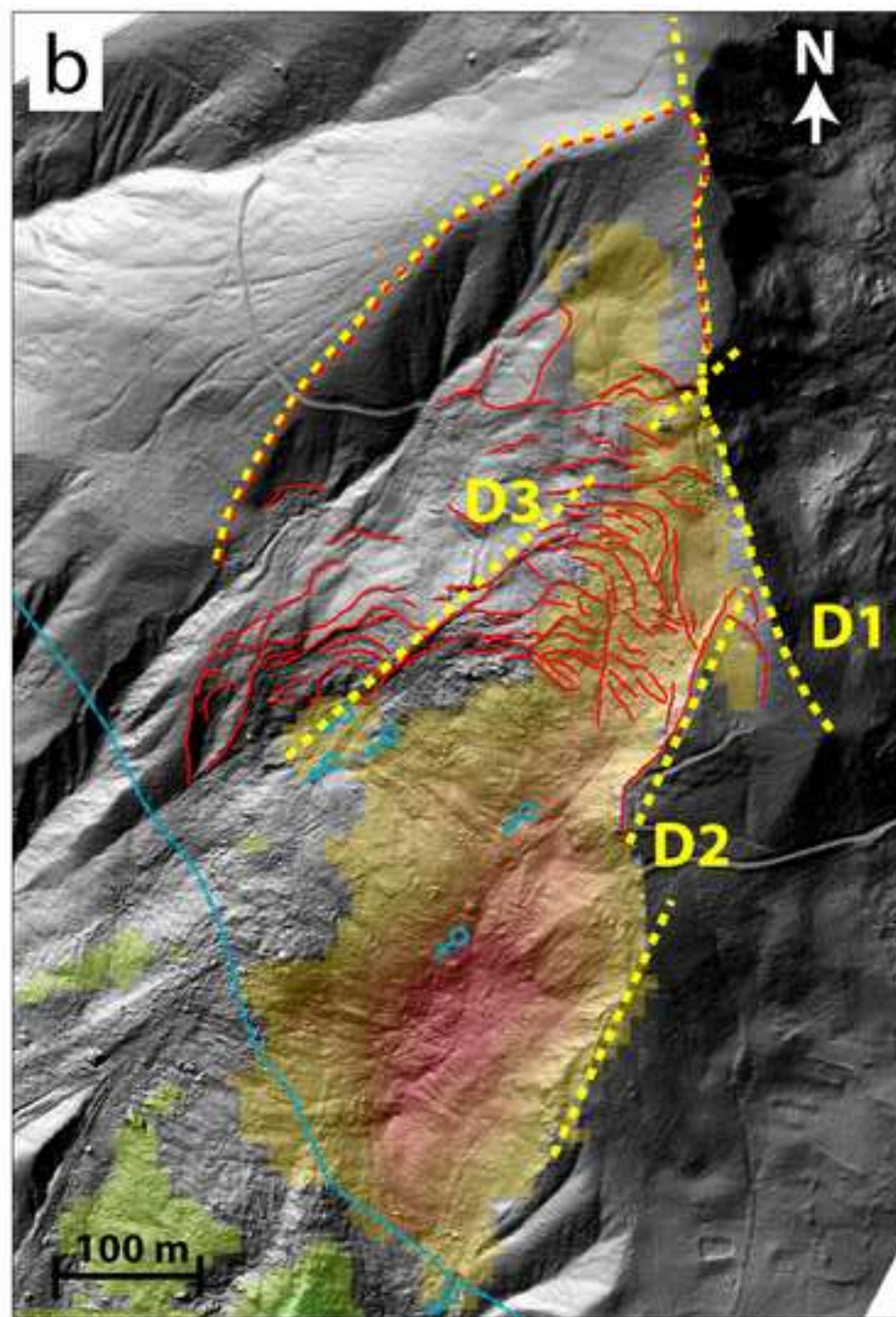
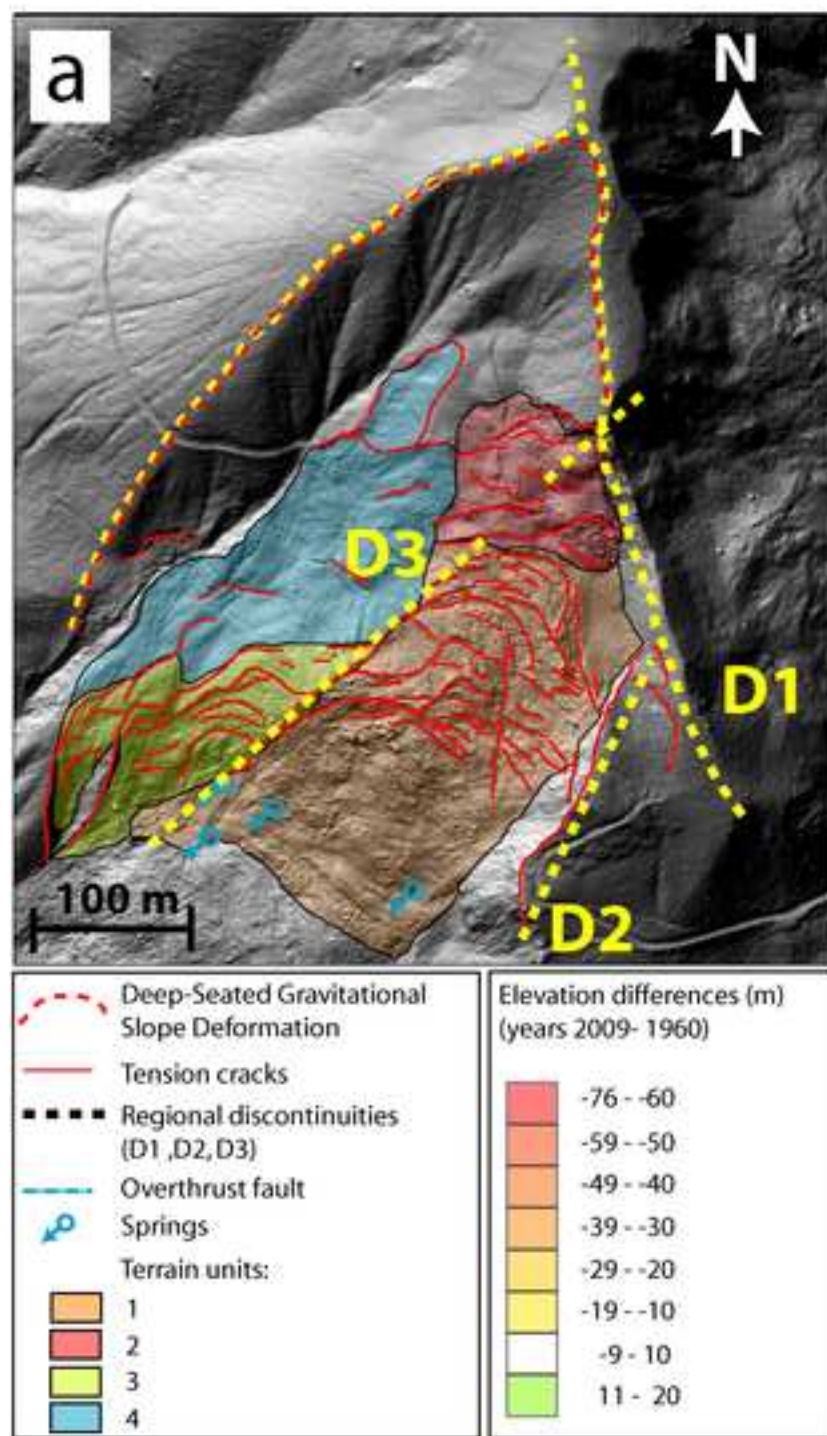


Figure 9
[Click here to download high resolution image](#)

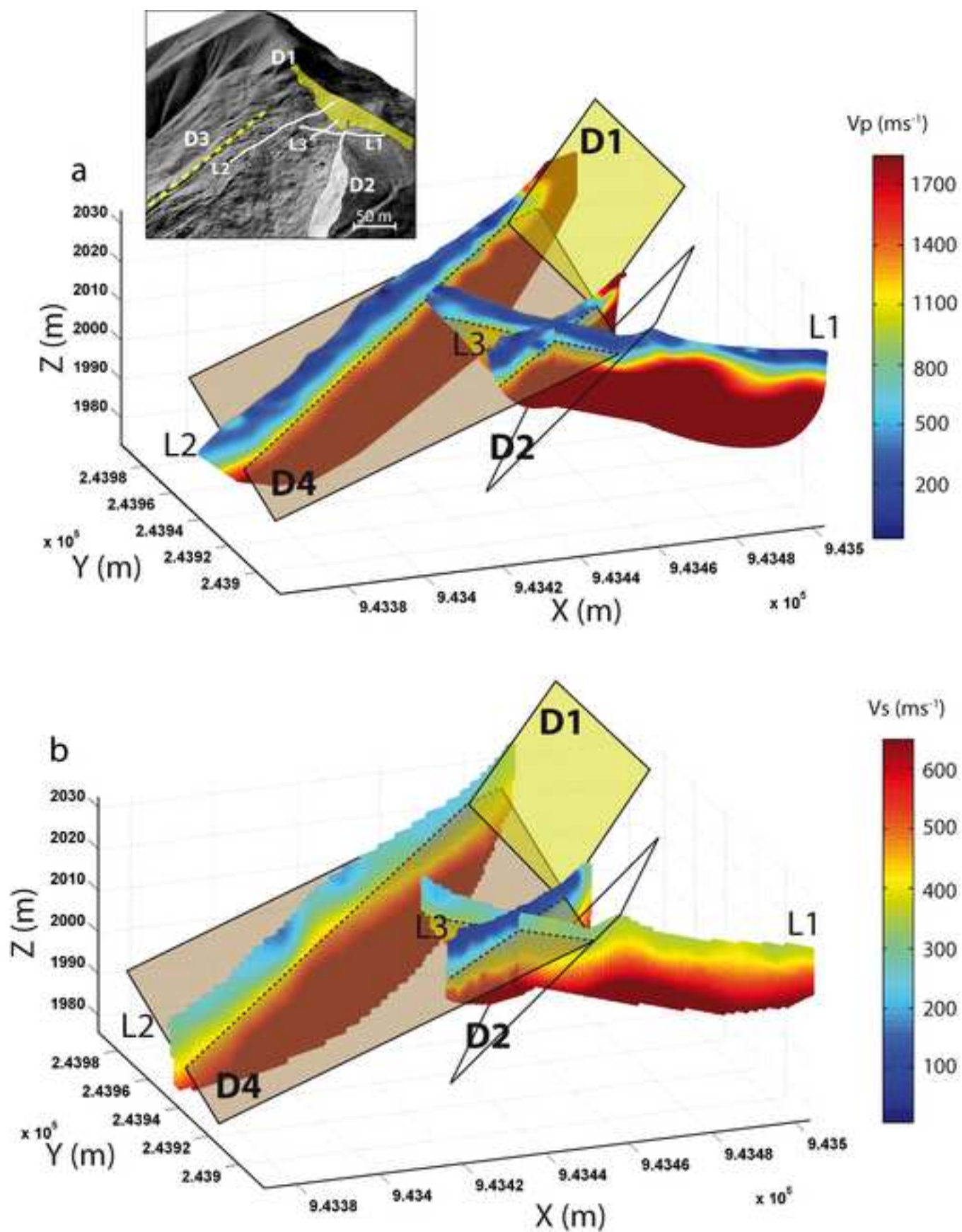


Figure 10
[Click here to download high resolution image](#)

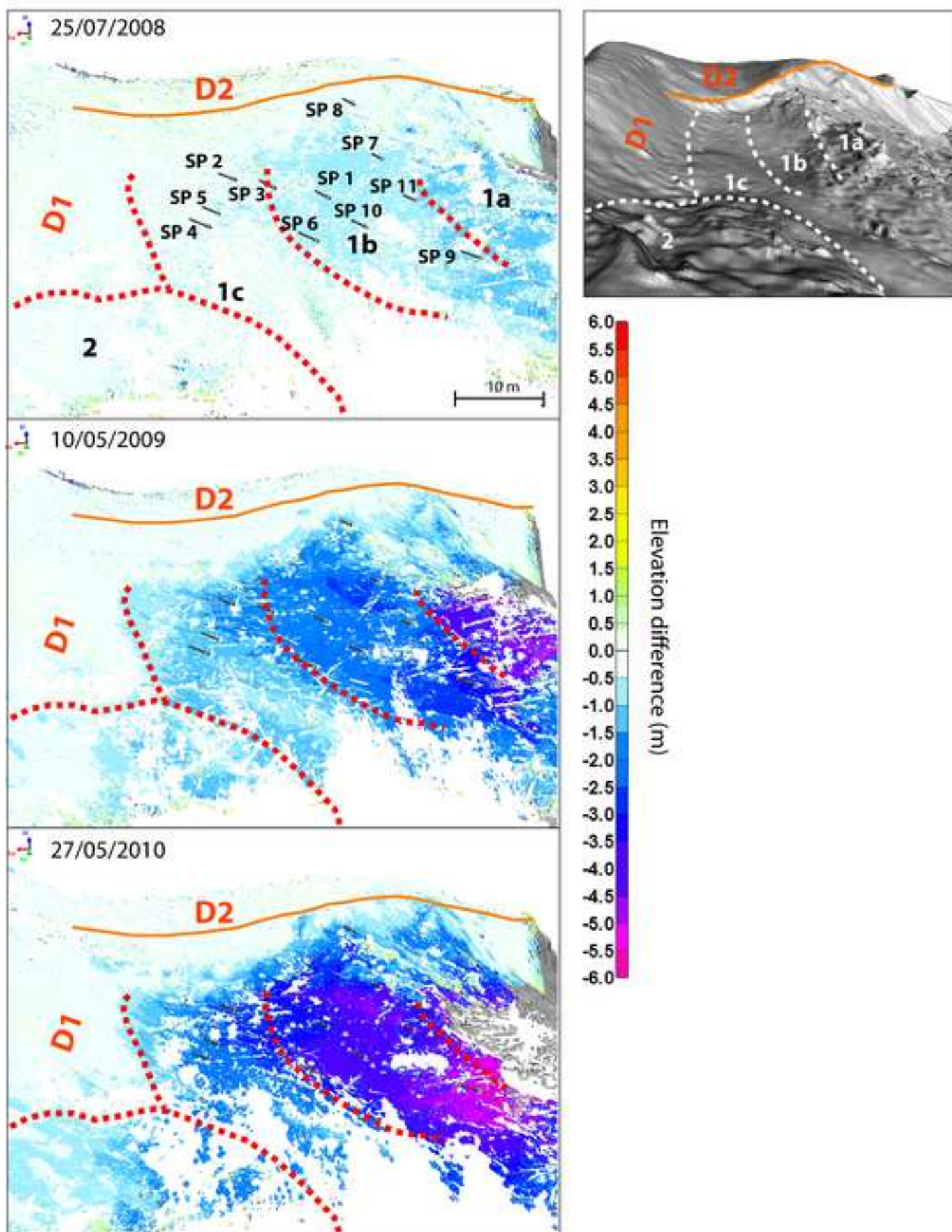


Figure 11

[Click here to download high resolution image](#)

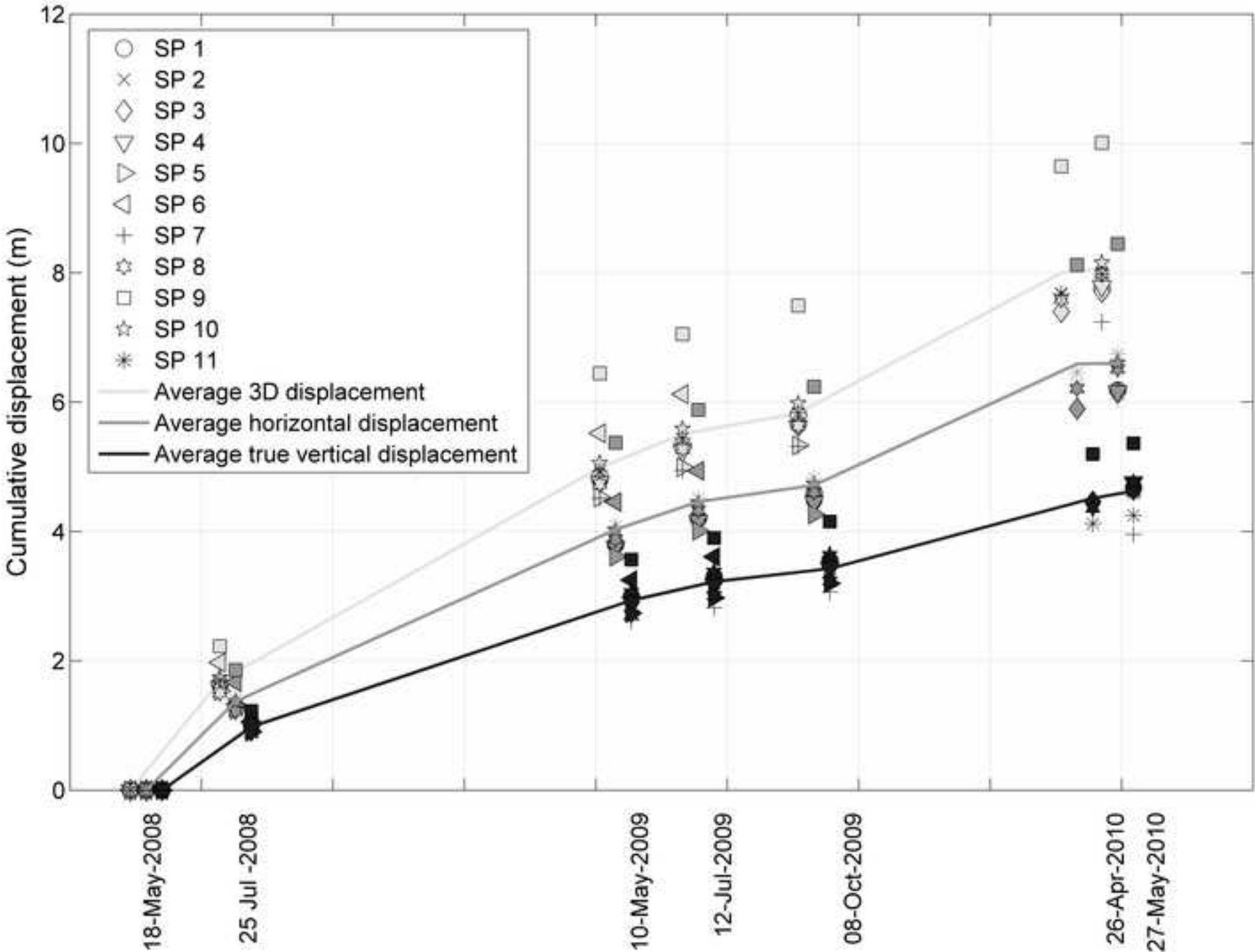


Figure 12
[Click here to download high resolution image](#)

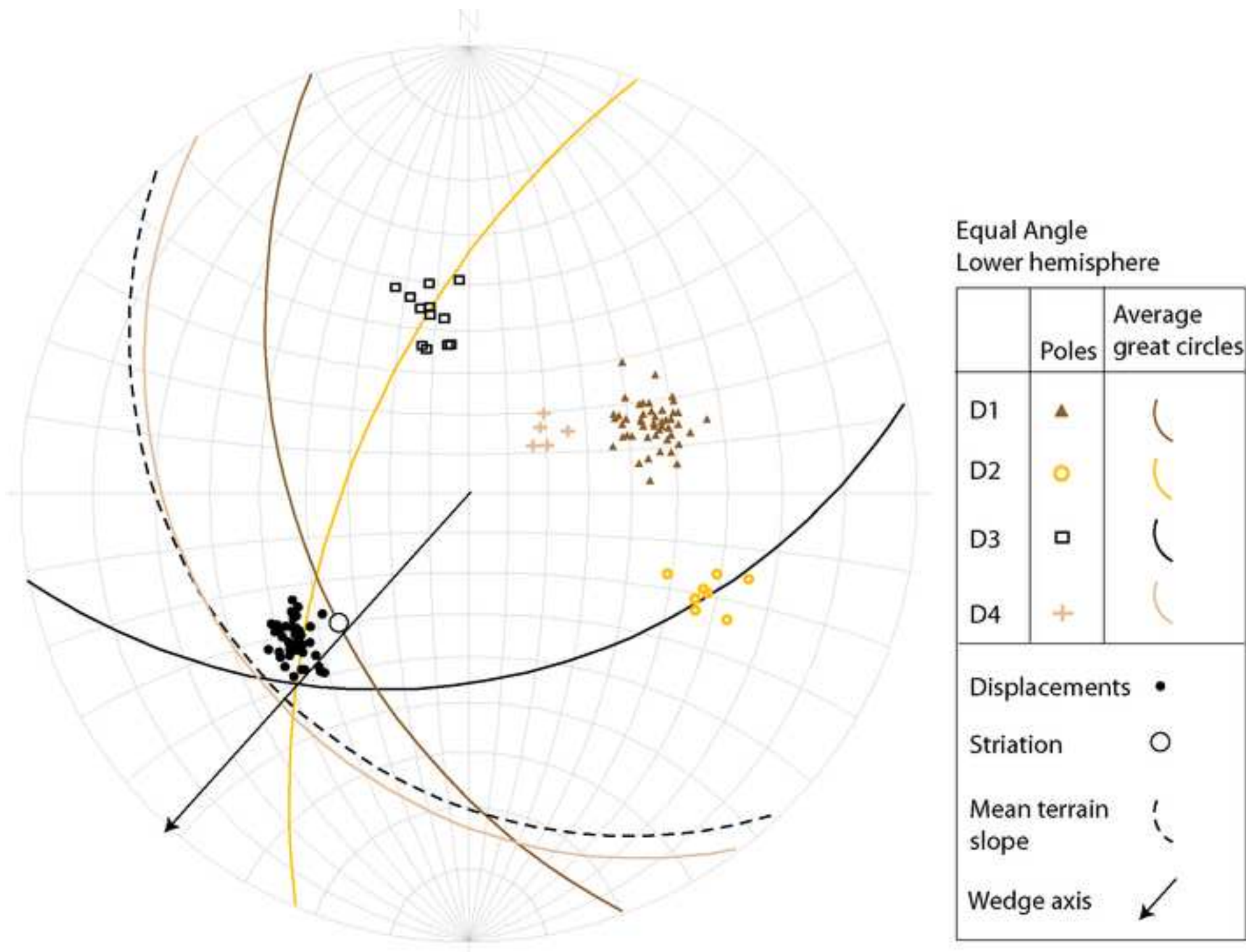


Figure 13
[Click here to download high resolution image](#)

